ISRN LUTMDN/TMHP—09/5197—SE
ISSN 0282-1990

CFD Simulations of Transport Processes including Chemical Reactions in SOFCs

Hedvig Paradis

Thesis for the Degree of Master of Science

Division of Heat Transfer
Department of Energy Sciences
Faculty of Engineering, LTH
Lund University
P.O. Box 118
SE-221 00 Lund
Sweden

LUNDS UNIVERSITET
Lunds Tekniska Högskola

CFD Simulations of Transport Processes including Chemical Reactions in SOFCs

Hedvig Paradis

Thesis for the degree of Master of Engineering, 2009

Division of Heat Transfer
Department of Energy Sciences
Faculty of Engineering (LTH)
Lund University

www.energy.lth.se

Abstract

Fuel cells are electrochemical devices that convert the chemical energy stored in the cell directly into electrical power. One type of fuel cell is the solid oxide fuel cell (SOFC), which is high-operating-temperature fuel cell. This makes it possible to reform hydrocarbon fuels internally. Internal reforming increases the applicability of different types of fuel. However, since they operate at very high temperatures (800–1100°C), material performance and manufacturing cost are concerns. It is possible to improve the performance of SOFCs by adopting a porous, anode-support structure to reduce the thickness of the electrolyte. Such a structure can operate at moderate temperatures of 600–800°C, while still providing an internal reforming environment.

The purpose of this study is to investigate the interaction between internal reforming and transport processes by implementing a CFD-model. It divides into two parts. Firstly, the current literature on the modelling of transport processes and chemical reaction mechanisms in SOFCs is reviewed and special emphasis is given to the description of Andersson's anode-supported SOFC model. Secondly, Andersson's model is extended by applying different global internal reforming reaction schemes and a comparison between the different models in terms of reaction rates and effects on the transport processes is carried out. Two different kinetics models are selected for the catalytic steam reforming reaction and the same equilibrium water-gas shift reaction is used throughout the model. The models developed are based on the governing equations of momentum-, heat- and mass transport. The models have been implemented in the COMSOL Multiphysics, based on the Finite Element Method. This software is designed for multiscale modelling, e.g. coupling different physical models at different scales. In this study the equations are solved simultaneously. A parameter study by varying the inlet temperature and surface area ratio is also conducted.

The base case showed that Achenbach & Riensche's model has a slower steam reforming reaction rate than Leinfelder's model, in which both the partial pressure for methane and water was concluded. Further, Leinfelder's model has a much higher pre-exponential value for the steam reforming reaction rate. This was revealed in the results for the temperature profiles as well as the reaction rates. The temperature decrease close to the inlet for Achenbach & Riensche's model was at about 10 K and for Leinfleder's model at about 45 K. The steam reforming reaction rate is more than 60 times faster for Leinfleder's model than for Achenbach & Riensche's model. For the parameter study, the effect of the temperature change for Achenbach & Riensche's model primarily had an effect on the reaction rates. The steam reforming reaction rate was more than doubled when the inlet temperature increased from 1050 K to 1150 K. The effect of the surface area ratio had similar effects on the temperature distribution and the reaction rates. The temperature increased faster for a higher surface area ratio and reached a higher maximum value. When the surface area ratio was doubled the maximum value for the steam reforming reaction rate was almost doubled. The results for Achenbach & Riensche's model were compatible with the results from Andersson [1]. The steam reforming reaction rate for Achenbach & Riensche's model was somewhat faster. The steam reforming reaction rate for Leinfelders's model was significantly faster. This brought the conclusions to the same as between Achenbach & Riensche's model and Leinfelder's model.

Acknowledgements

This work has been carried out at the Division of Heat Transfer, Department of Energy Sciences, Lund University, Sweden.

I would like to thank my supervisors Associate Professor Jinliang Yuan and Martin Andersson as well as Professor Bengt Sundén for support during my work. I would also like to thank everyone at the Division of Heat Transfer for great support, guidance and good discussions during my whole time at the Division.

Finally, I would like to express my gratitude and thanks to my family and friends for always being encouraging and supporting.

Table of contents

Nomenclature

C	fuel consumption, dimensionless
c_p	specific heat at constant pressure, J/(kg·K)
Da	Darcy number, dimensionless
D_{ij}	Maxwell-Stefan binary diffusion coefficient, m^2/s
D_i^T	thermal diffusion coefficient, kg/(m·s)
E	activation energy, kJ/mol
e	characteristic Lennard-Jones energy, K
F	volume force vector, N/m^3
F	Faraday constant, 96485 C/mol
h	enthalpy, kJ/mol
h_{sg}	heat transfer coefficient, $W/(m^2 \cdot K)$
h_v	volume heat transfer coefficient, $W/(m^3 \cdot K)$
i	current density, A/cm^2
i_0	exchange current density, A/cm^2
k	thermal conductivity, W/(m·K)
k_i	reaction rate constant, $mol/(m^3 \cdot bar^2 \cdot s)$
k'	Boltzmann's constant, J/K
k''	pre-exponential factor, $1/(\Omega \cdot m^2)$
K_e	equilibrium constant, Pa^2 or dimensionless
l_{ij}	characteristic length, Å
M	molecular weight of the mixture, kg/mol
M_j	molecular weight of species j, kg/mol
n_0	inlet mass flux, $kg/(m^2 \cdot s)$
n_e	number of electrons transferred per reaction, -
Nu	Nusselt number, dimensionless
p	pressure, Pa, bar
q	heat flux, W/m^2
Q	source term (heat), W/m^3
r	velocity effect due to electrochemical reaction, m/s
r_i	reaction rate, $mol/(m^3 \cdot s)$, $mol/(m^2 \cdot s)$
R	gas constant, 8.314 J/(mol·K)
SA	surface area ratio, m^2/m^3
S_i	source term for the reaction rate, $kg/(m^3 \cdot s)$
T	temperature, K
T	viscous stress tensor, N/m^2
t	tortuosity, dimensionless
u,v	velocity, m/s
w_i	mass fraction of species i, kg/kg
x, y	coordinate system, m
x_i	molar fraction of species i, mol/mol

Greek symbols

ε	porosity, dimensionless
η	over potential, V
κ	permeability, m^2
κ_{dv}	deviation from thermodynamic equilibrium, Pa·s
μ	dynamic viscosity, Pa·s
ρ	density, kg/m^3

τ	component thickness, m
Ω_D	diffusion collision integral, dimensionless

Subscripts

0	initial
a	anode
act	activation polarization
b	bulk
c	cathode
conc	concentration polarization
e	electrode, $e \in \{a,c\}$
el	electrolyte
f	fluid phase
g	gas phase
i	molecule i
int	interconnect
j	molecule j
K	Knudsen diffusion
losses	activation and concentration polarization
ohm	ohmic polarization
r	steam reforming reaction
por	porous media
s	solid phase, water-gas shift reaction
w	gas channel wall
+	forward reaction
-	reverse reaction

Abbreviations

CFD	computational fluid dynamics
FC	fuel cell
FEM	finite element method
FVM	finite volume method
IT	intermediate temperature
LTE	local thermal equilibrium
LTNE	local thermal non-equilibrium
PEMFC	polymer electrolyte membrane fuel cell
SOFC	solid oxide fuel cell
TPB	three-phase boundary
YSZ	yttria-stabilized zirconia

Chemical

CH_4	methane
CO	carbon monoxide
CO_2	carbon dioxide
H_2	hydrogen
H_2O	water
O_2	oxygen
Ni	nickel

1 Introduction

After some time of decreasing interest, fuel cell research is now receiving a lot of attention. The reason for its revival is that researchers of energy systems consider fuels cells as a promising future resource for both stationary and distributed electric power stations because of their high performance and high reliability [1, 2]. In spite of the fact that a lot of work has already been carried out on fuels cells in general, there are still areas that need a great deal of further exploration – two of them are to increase the life time and lower the production cost [1]. In order to explore these aspects in greater depth, there is a need for both multiphysics modelling and multiscale modelling. This has to be done by solving equations for momentum-, heat- and mass transport and chemical reactions at the same time.

Solid oxide fuel cells (SOFCs) are particularly interesting because they operate at high temperatures and can therefore handle the reforming of hydrocarbon fuels directly within the cell. SOFCs have a number of advantages, e.g. high conversion efficiency, high quality exhaust heat and flexibility of fuel input. However, as expected, SOFCs also have disadvantages. For instance, since they operate at very high temperatures (800–1100°C [3]), material performance and manufacturing cost may be a concern. Recently, attempts have been made to lower the operating temperature of SOFCs by adopting a porous, anode-supported structure to reduce the thickness of the electrolyte. Such a structure can operate at moderate temperatures of 600–800°C [3], while still providing an internal reforming environment which increases the applicability of different hydrogen-rich fuels. Andersson [1] developed a model for an anode-supported SOFC to study species concentration, temperature distribution and further extended the model for internal reforming.

The purpose of this study is to further extend Andersson's model of the anode-supported SOFC to get a deeper understanding the effect of the internal reforming of methane on the transport processes. It has been suggested in the literature that a crucial factor for the performance of SOFCs is how methane is reformed internally by steam in porous environments [3]. SOFC physics can be considered and presented differently according to different scales. This investigation involves various length scales, primarily macroscales but in part also microscales. A microscale corresponds to atom or molecule level, and macroscales correspond to the global flow field. Internal reforming depends on microscale catalyst distribution and surface chemical reactions, which affect transport processes at a macroscopic level. It is necessary to model SOFCs, in order to fully understand how different parameters affect the performance, by connecting different physical phenomena at different scales.

1.1 Research objectives

The aim of this thesis is two-fold. Firstly, a description of current research on modelling of chemical reaction mechanisms involving Ni catalyst material structures and of effects on transfer processes in electrodes and electrolytes of SOFCs is provided. Secondly, a consideration of models, based on an extension of Andersson's model of anode-supported SOFC, is presented by applying different global internal reforming reaction schemes. They are subsequently compared in terms of reaction rates and effects on the transport processes.

1.2 Methodology

In order to analyze the electrochemical reactions and transport processes in SOFCs, an extension of Andersson's two-dimensional computational fluid dynamics approach for a single cell is developed. In his study, Andersson developed a model for an anode-supported SOFC. An extended version including internal reforming reactions was created and a comparison was carried out between the basic model and the extended model. The present contribution is a comparison between different global reforming schemes for methane as fuel. These processes were implemented in the commercial software COMSOL Multiphysics (version 3.5a), based on the Finite Element Method. This software is coded for multiscale modelling, e.g. coupling different physical models at different scales. A parameter study was carried out to investigate the effect of change in temperature and pressure for the system.

The computational domain includes air and fuel channels, anode, cathode, electrolyte and interconnects from a single unit cell. Conservation of momentum-, heat- and mass transfer equations are strongly connected, and these equations are solved simultaneously. The model of this study considers the porous electrodes and gas flow channels at a macroscopic level and takes into account the microscopic effects at pore and molecular level for the thin active layers and electrolyte. The internal reforming of hydrocarbon fuel is modelled by different global reforming schemes for the chemistry in the porous anode. The schemes are then compared based on reaction rates and effects on the transport processes. Two different kinetics models are chosen for the catalytic steam reforming reaction, and the equilibrium water-gas shift reaction is used throughout the model. An evaluation of the different kinetic models is carried out. A parameter study is also conducted in terms of changing the inlet temperature for the air and fuel channels as well as changing the surface area ratio.

1.3 Thesis outline

Chapter 1 contains a short presentation of the thesis. Chapter 2 gives an overview of the relevant literature and a general description of SOFCs. A detailed explanation of the mathematical model is presented in Chapter 3 with governing equations, boundary conditions, sources terms and variable modification of the reforming reactions. The results are presented in Chapter 4 and finally Chapter 5 provides conclusions drawn from the results.

2 Literature review

The fuel cell was invented in 1838-39 by C. F. Schönbein at Basel University and simultaneously by W. R. Grove at the Royal Institution of Great Britain. Today fuel cell research attracts a lot of interest due to the possibility of achieving electrical power in an efficient and clean manner. The number of scientific articles published has increased tremendously since 2000 [1]. In spite of the increase, research on fuel cells is still in its infancy of development.

Fuel cells are energy conversion devices, which produce electricity and heat directly from a hydrogen-based fuel through electrochemical reactions when the device is fed with an oxidant. Fuel cells do this in one step and differ from conventional heat engines where this process unfolds in several steps. The heat engine's major loss of efficiency is the conversion of thermal energy to shaft work. The heat engine is limited by the efficiency of the Carnot cycle [4]. Since the step from thermal energy to shaft work is not included when a fuel cell converts energy to electrical power, this reduction gives a significant difference in efficiency between a heat engine and a fuel cell.

There are several different types of fuel cells. They are generally divided into two groups, low and high temperature cells and named according to the material used for the electrolyte, i.e. solid oxide fuel cell (SOFC) and proton exchange membrane fuel cell (PEMFC). A single SOFC consists of an air channel and a fuel channel, two porous electrodes which are separated by an electrolyte. The fuel electrode is the anode and the oxidant electrode is the cathode. The electrolyte works partly as a connection for the external electrically conducting circuit, which lets the electrons pass through, and partly as a passage for the ions and blockage for the electrons. The oxygen ions react with hydrogen and carbon monoxide in the fuel mixture at the anode/electrolyte interface and produce water and carbon dioxide while releasing electrons that flow via external circuits to the cathode/electrolyte. The electrolyte should not be permeable for gas, but the porous electrodes should be permeable for gas and liquid. The anode is usually nickel/zirconia cermet which provides high electrochemical performance and good chemical stability and the cathode is usually a perovskite material. A schematic illustration of a SOFC fed with hydrogen as fuel is shown in Fig. 1.

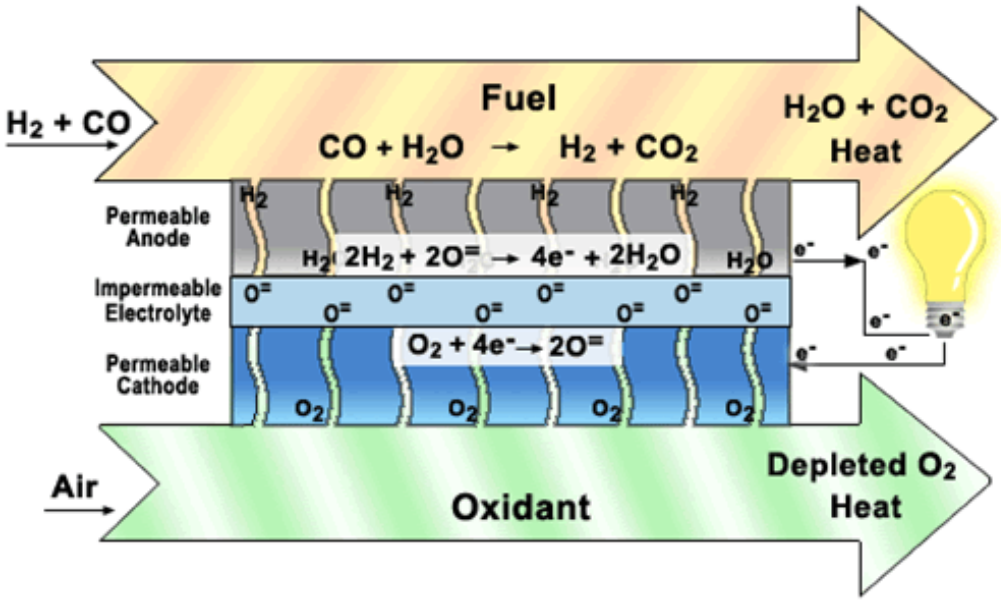

Figure 1: Schematic SOFC [7]

This study is concerned with the internal reforming of methane in SOFCs. Because SOFCs operate at high temperature, they supply a sufficiently good environment to internally reform the hydrocarbon-based fuel within the cell. For this reason it is possible to work with a broader variety of fuels, e.g. methane and propane [2]. This gives the SOFCs a major advantage because pure hydrogen is highly flammable and volatile which makes it problematic to handle. Also, hydrogen has low density, which makes storing costly [4]. It should also be mentioned that pure hydrogen is difficult to obtain since it has to be extracted from another source, most commonly natural gas. The overall global reactions are stated below. More detailed surface reactions can be found in the literature [5, 6].

$$O_2 + 4e^- \Leftrightarrow 2O^{2-} \quad (1)$$

$$H_2 + O^{2-} \Leftrightarrow H_2O + 2e^- \quad (2)$$

$$CO + O^{2-} \Leftrightarrow CO_2 + 2e^- \quad (3)$$

$$CH_4 + H_2O \Leftrightarrow 3H_2 + CO \quad (4)$$

$$CO + H_2O \Leftrightarrow H_2 + CO_2 \quad (5)$$

Eq. (1) is the reduction of oxygen in the cathode. Eq. (2) and (3) are the electrochemical reactions at the anodic TPB (Three-Phase Boundary). TPB is the region where the electrolyte and electrode meet. Eq. (4) is the steam reforming of methane, which needs to be carried out before the electrochemical reactions, and which is usually called catalytic steam reforming reaction. Carbon monoxide can be oxidized as in eq. (3) or react with water as in eq. (5). Eq. (5) is often called water-gas shift reaction.

The configuration of SOFC is usually planar or tubular, and can be electrolyte-, anode- or cathode supported. If the case is electrode-supported (anode or cathode), it means that the thickest part is the electrode (either anode or cathode depending on the configuration) and that part works as the supporting structure. Similarly, the electrolyte is the thickest and supporting part for the electrolyte-supported configuration. In this thesis an anode-supported configuration is adopted to keep the electrolyte thin. As mentioned before this structure makes it possible to reduce the temperature to a moderate level (600–800 ºC [3]) and these fuel cells are classified as intermediate temperature solid oxide fuel cells (ITSOFCs).

2.1 Review of Andersson's work

Andersson (2009) [1] started out by developing a basic two-dimensional model for an anode-supported SOFC. Equations for momentum-, heat- and mass transport were all solved at the same time. Andersson also created an extended model, which differed from the basic model in that it included internal reforming reactions. However, the models, both the basic and the extended, were two-dimensional only, and the connection between the electrodes and interconnects cannot be explicitly observed because of the cross-sectional choice. The choice of configuration is shown in Fig. 2. The remaining part of this section provides a description of Andersson's equations, assumptions and results.

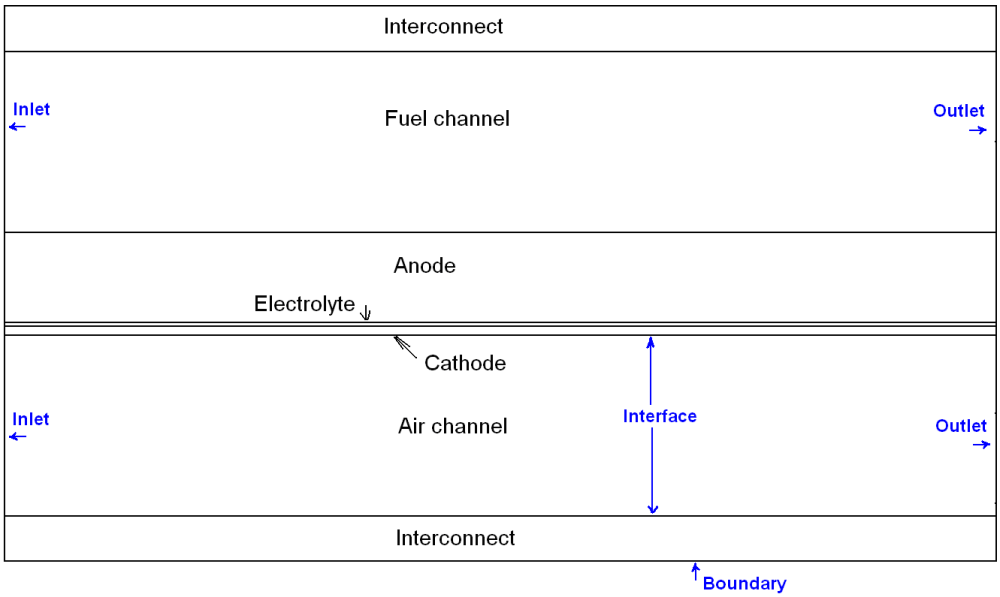

Figure 2: Schematic of the anode-supported SOFC model [1]

Andersson described two procedures to solve the electrochemical reactions in the governing equations. In the first procedure, the reactions were defined as source terms in the governing equations and in the second procedure as interface conditions defined at the electrode/electrolyte interfaces. Due to the thin active layer (compared to the electrode), Andersson assumed that the electrochemical reactions take place at the interfaces between the electrode and the electrolyte which further affect the governing equations.

Andersson, then, used the Darcy-Brinkman equation for treating the gas flow in the porous electrodes, fuel and air channels for the momentum transport equation. The reason for expanding the Darcy equation and the Navier-Stokes equation to the Darcy-Brinkman equation was to better define interface conditions between two domains as well as the tangential velocity component. The boundary conditions for the momentum equation were defined as laminar flow at the inlet of the fuel and air channels with an average flow rate. The outlet conditions were defined as: $\mu\left(\nabla u+(\nabla u)^{T}\right)\cdot n=0$ and $p=p_0=1\text{atm}$. The interfaces were defined as walls ($u=0$), and between the porous electrodes, fuel and air channels were defined as continuous. The entry effects for the flow profile were neglected. As the interface between the cathode and electrolyte depends on the gas velocity, that was also calculated. The effect of the gas velocity is due to the electrochemical reactions, which in turn depend on the current density and consumption of oxygen. At the interface between anode and electrolyte, the water produced and hydrogen consumed affect the interface conditions through the reactions.

To describe the mass transport for the gases within the cell, Andersson used the Maxwell-Stefan equation for mass diffusion and convection. The Maxwell-Stefan equation is a simplified version of the Dusty Gas Model since the Knudsen diffusion was neglected. Due to this, the computational cost can be reduced. The boundary conditions for the mass transport equation were defined as specified mass fraction at the gas channel inlet and the boundaries. The interfaces between the interconnects and the gas channels were also defined because the governing equation for mass transport does not solve that.

The temperature distribution was calculated separately for the gas phase (fuel, air) and solid phase (interconnects, electrodes, electrolyte). The general heat conduction equation was solved for the temperature distribution in the solid phase. Furthermore, the temperature distribution for the gas mixtures in the porous electrodes, fuel channel and air channels were calculated from:

$$\nabla(-k_g \cdot \nabla T_g) = Q_g - \rho_g \cdot c_{p,g} \cdot u \cdot \nabla T_g \quad (6)$$

where $c_{p,g}$ is the gas phase specific heat, k_g the thermal conductivity for the gas phase, ρ_g the gas phase density, T_g the temperature in the gas phase and Q_g the heat transfer between the gas phase and the solid phase. The heat transfer boundary conditions were defined separately for the gas- and solid phase. The outlet conditions for the gas channels were defined as a convective flux. The boundaries at the top and the bottom were defined as symmetric because it was assumed that the cell is surrounded by other cells at the same temperature distribution. The value for the Nusselt number was based on a fully developed flow for a rectangular duct with aspect ratio 1 and was set as a constant. Heat is generated by the electrochemical reactions, i.e. polarization losses at the electrodes/electrolyte interfaces. The concentration and activation losses were also defined.

Andersson extended his basic model to include the reforming reactions. The five species: hydrogen, carbon monoxide, carbon dioxide, methane and water, were considered at the fuel side. Due to high temperatures, the steam reforming reaction which converts methane into hydrogen and carbon monoxide is fast. For the momentum equation the density, dynamic viscosity and thermal conductivity were all updated to cover the five species. In the Maxwell-Stefan equation for mass transport, the reforming chemistry was specified as a source term and on the fuel side it was updated to include interactions between the five species. The Maxwell-Stefan diffusion coefficient was also modified to handle the five species. Nickel/Zirconia was used as the anode material in the model because it can supply sufficient activity for the steam reforming reactions. Global reforming reactions from [8] were used for the steam reforming and the water-gas shift reactions. The heat generation and consumption, due to the reforming reactions, were defined as source terms. Heat consumption and generation were assumed to occur on the solid surface involving the catalytic reaction. These assumptions were based on the characteristics for an SOFC anode with a nickel catalyst.

In addition, a parameter study was conducted to investigate the temperature difference between the solid and the gas phase when the surface area and heat transfer coefficient (between the gases and walls) changed.

2.1.1 The Result for the Basic Model

The flow direction was set from left to right and the temperature increase along the main flow direction (the x-direction). The non-uniform temperature distribution in the y-direction occurred because the convective heat flux was greater in the air channel than in the fuel channel due to a larger flow rate. As a result the mole fraction of oxygen decreased in the air channel and the cathode. The flow was forced towards the cathode/electrolyte interface because there was a concentration difference in the y-direction. The mole fraction hydrogen decreased along the flow direction in the fuel channel and caused the hydrogen molecules in the y-direction to approach the anode/electrolyte interface. The ohmic polarization losses in the electrodes and concentration polarization were negligible compared to the activation and the ohmic polarization in the electrolyte. They decreased along the main flow direction as the temperature increased. A larger surplus of oxygen cooled down the cell. This proved to be an easy way to control the temperature increase in the cell. A higher surplus factor brought a reduced temperature increase in the main flow direction and also a reduced concentration polarization in the y-direction. An increased inlet temperature gave a reduced temperature increase along the main flow direction which was mainly due to the fact that the ohmic and activation polarization decreases. An increase of the current density increased the ohmic and the activation polarizations which made it possible to reduce the fuel cell stack size at the cost of heat generation. The decrease in ionic

conductivity in the electrolyte made it more difficult for the oxygen ions to pass through the electrolyte.

2.1.2 The Result for the Extended Model

When methane reacted with steam at the Ni-catalyst surface in the porous anode, carbon monoxide and hydrogen were produced. Hydrogen was consumed at the anodic TPB due to the electrochemical reactions. The water-gas shift reaction was in equilibrium wherever the gases were present. The steam reforming reaction decreased the temperature close to the fuel channel inlet. The temperature on the air side was slightly lower due to the higher air flow rate. The concentration difference in the y-direction was an effect of the consumption of methane in the porous layer. Mole fraction of hydrogen increased as methane and carbon monoxide was catalytically converted into hydrogen. Carbon monoxide was generated in the porous anode structure as methane was reformed and then gradually converted to hydrogen and carbon dioxide. The concentration difference in the y-direction close to the inlet was due to the fact that methane reforming took place in the anode only. The reaction rate for the steam reforming depends among other things, on the temperature and concentration. A higher operating temperature gave a higher reaction rate. The use of a hydrocarbon fuel decreased the temperature inside the fuel cell compared to if pure hydrogen was used.

2.2 Transport processes

As mentioned before, it is essential to connect the different transport processes when modelling SOFCs. The transport of fuel gases to the active surface for the electrochemical reactions are governed by different parameters, such as porous microstructure, gas consumption, pressure gradient between the fuel flow duct and the porous anode, and finally the inlet conditions [9]. The gas molecules diffuse to the TPB, where the electrochemical reactions take place. The hydrogen concentration depends on the transport within the porous anode and the heterogeneous reforming reaction chemistry [1].

2.2.1 Mass transport

In the electrodes, mass transfer is dominated by gas diffusion and the transport takes place in the gas phase, which is influenced by the electrochemical reactions at the solid surface at the active TPB [10]. The appropriate mass flow rate of the fuel and the oxidant depends on the electrochemical reaction, temperature, pressure and internal reforming [11, 12]. The flow of electronic charge through the external circuit balances the flow ionic charge through the electrolyte and electrical power is produced. Consequently, it is important to consider the electron transport where the current is produced from [13].

Mass transport can be calculated using Fick's law, which is the simplest diffusion model. But in the literature for a multi-component system, similar models to the Stefan-Maxwell model are often implemented to calculate the diffusion [14, 15]. Furthermore, when extended with the Knudsen diffusion term to predict the molecules collision effect it is usually called the Dusty Gas model [2, 5, 11]. Suwanwarangkul et al. [16] compared Fick's, the Dusty Gas and the Stefan-Maxwell models by analyzing the concentration potential. It was found that the Dusty Gas model is the most appropriate for modelling gas transport. It was also demonstrated that the Dusty Gas model is suitable for a multi-component system. Other researchers, such as Aguiar et al. [17], focus on the mass transport of the active species including the electrochemical processes [18].

2.2.2 Heat transport

Knowledge of the heat transfer processes is required because the current and temperature distributions are strongly connected in fuel cells. The heat transfer inside SOFCs involves various features, such as [14]:

- Convective heat transfer between the solid surfaces and the gas channels.
- Conductive heat transfer in the solid and the porous structures.
- Radiation between different surfaces.[1]

For heat conduction Fourier's law is used and Newton's law is used for heat convection. Over the years researchers have made different assumptions when modelling heat transfer in SOFCs. The heat transfer coefficients are determined through Nusselt number. Commonly, Nusselt number is assumed to be independent of Reynolds number, given that it is a fully developed laminar flow [4, 17]. Heat generation occurs due to the electrochemical reactions at the active surfaces. A greater portion of heat generation within a SOFC is produced near the interface between the electrode and electrolyte [20]. It also occurs due to the internal reforming of methane in the porous anode [14].

In order to be able to predict and optimize the overall performance as well as avoiding thermo-mechanical degradation, it is very important to accurately predict the temperature. For the temperature distribution, it is common in the literature to assume local thermal equilibrium (LTE) [12, 20]. A local non-equilibrium approach was developed in [20] to model the temperature difference between the solid phase and the gas phase within the porous electrodes. The temperature distribution here is calculated on the basis of the local thermal non-equilibrium (LTNE) approach, separately for the gas- and solid phase. Effective transport parameters for the porous structure need to be calculated when an LTE approach is used. This is not needed for the LTNE approach because it is evaluated at every cell throughout the meshing domain.

2.2.3 Momentum transport

The governing equations for momentum transport are the Navier-Stokes equation in channels and the Darcy equation for the porous electrodes [9, 12]. It is common to assume laminar flow for the channels due to low velocities. This measure decreases the computational cost significantly [19]. The Darcy equation describes the balance between the force from the pressure gradient and the frictional resistance from the solid material. Further, the equation can be modified with the Brinkman term to make it possible to model boundary/interface conditions. Because no-slip at neither walls nor the resulting boundaries is well described with the basic Darcy equation, the Darcy-Brinkman equation is preferred [2].

The momentum equation has also been disregarded in cases, due to the assumption of constant pressure, which saves computational cost. This assumption has been adopted by researchers to give similar results to those studies without this assumption [19].

2.3 Internal reforming

The internal reforming offers some advantages compared to an external pre-reformer. There is less need for cooling of the cell and less steam needed for the reforming reactions. The entropy losses of the direct oxidation of CH_4 are small resulting in a high thermodynamic efficiency of $\eta = 99.7\%$ [21]. Unfortunately, it also comes with some disadvantages. Because the reaction process is very fast, this results in large temperature gradients that may lead to thermal tensions

[1] Radiation is not included in this thesis because the impact is assumed to be negligible [19].

and construction problems. This can be solved by lowering the operating temperature, within the intermediate range, to reduce steam reaction rates [22]. On the other hand, the conversion of methane to hydrogen and carbon monoxide works efficiently because of the high operating temperature. The heat, generated by the electrochemical reactions (exothermic) at the active surface, is consumed by the steam reforming reactions [23].

The reaction rates for the internal reforming reactions can be described by either simplified global expressions or detailed surface chemical expressions. One of the main goals of this thesis is to compare different internal reforming reaction schemes, and therefore only global expressions will be investigated. Detailed surface chemistry can be found in the literature [5, 6]. For the global schemes, methane is converted to hydrogen and carbon monoxide in one step inside the porous anode with catalytic steam reforming. This is represented by eq. (4) and called the catalytic steam reforming reaction. The steam reforming is endothermic and the water-gas shift reaction is exothermic. However, their combined effect is endothermic [19]. Several researchers consider the steam reforming and the water-gas shift reaction to reach equilibrium inside the cell [4]. The reaction schemes are divided into equilibrium models and kinetic models. Some researchers claim that equilibrium cannot be assumed for the steam reforming reaction but it can be appropriate for the water-gas shift reaction. This is based on the fact that the steam reforming reaction kinetics are slow compared to both shifting and hydrogen electrochemical oxidation [4].

In the literature the different global models vary quite a lot with respect to the assumption about the steam reforming reaction. Firstly, as mentioned before, there are different views on if the steam reforming reaction reaches equilibrium or not. Secondly, the applied kinetics models for the steam reforming reaction can have rather different dependency of pressure [24]. Besides the disagreement with regard to the dependency of the methane reforming rate on the partial pressure of the reactants, there are also differences for the reported activation energies range from 60 to 230 kJ/mol [25]. The reaction rates, which are the concerns in this thesis, will be implemented in the Maxwell-Stefan equation for mass transport as source terms according to [14]:

$$S_{H_2} = (3r_r + r_s) \cdot M_{H_2} \tag{7}$$

$$S_{CH_4} = -r_r \cdot M_{CH_4} \tag{8}$$

$$S_{H_2O} = (-r_r - r_s) \cdot M_{H_2O} \tag{9}$$

$$S_{CO} = (r_r - r_s) \cdot M_{CO} \tag{10}$$

where M_i is the molecular weight of the species i, and S_i the source term. The equation for CO_2 can be solved separately because the sum of the mass fractions is equal to unity. The reaction rate r_r is for the catalytic steam reforming reaction and r_s for the water-gas shift reaction. An important aspect of generation of steam reforming kinetics data on Ni-based anodes is that they are prone to carbon deposition. To handle this issue, the catalyst is modified by the addition of certain compounds that impart resistance to carbon formation. One major criticism on the reported work on internal reforming kinetics is that it has been carried out using catalysts forms and manufacturing processes that are not used in SOFC [25]. Small changes during the process of manufacturing can have an effect on the catalytic characteristics. A characteristic, such as the corn size distribution, has a strong influence on the anodes catalytic, electro and electrochemical characteristics [26]. This is not always clearly stated in the literature which makes it hard to reproduce results numerically.

2.4 Electrochemistry

H_2 and CO participate in the charge transfer chemistry, but the rate at which CO is converted in the water-gas shift reaction is much faster than the rate of the electrochemical oxidation of CO. CO can often be neglected because H_2 dominates when both are present in the system [23]. The electrochemical reactions take place at the TPB, i.e. the interfaces between the electrodes and the electrolyte. They are described in eq. (2) and eq. (3). A larger TPB gives more reaction sites. The importance of the TPB area increases when a thin electrode is applied [1]. The influence of the electrochemical reactions on the gas mass balance is here represented by the mass flux rate (mol/m^{2}s), which is defined for the different species as:

$$r_{H_2} = \frac{-i}{2F} \tag{11}$$

$$r_{H_2O} = \frac{i}{2F} \tag{12}$$

$$r_{O_2} = \frac{-i}{4F} \tag{13}$$

where i is the current density and F is the Faraday constant [1, 2]. The mass flux rates above are defined for use of pure hydrogen. The mass flux rate represents the absorption of reactants and generation of products and is related to the local current density.

At the active surface, heat generation occurs due to the electrochemical reactions and the cell losses. The heat generation is defined as:

$$q_b = \frac{-i}{2F} \cdot \Delta H_{H_2O} \cdot M_{H_2O} - i \cdot V_{cell} \tag{14}$$

where ΔH is enthalpy of formation for water. The first term on the RHS in eq. (14) accounts for the amount of heat released by the water formation, and the second term accounts for the current density generated by the electrochemical reactions [14].

Voltage losses reduce the ideal voltage calculated by the Nernst equation and these voltage losses are often referred to as polarizations. They are classified into three groups: ohmic, activation and concentration. Ohmic polarization appears due to the internal resistance to electronic/ionic charge transport. Activation polarization appears due to the potential drop associated with the electrochemical reactions involved. Finally, the concentration polarization is due to the effect of slow mass diffusion through the porous electrodes to reaction sites and back to the gas flow [4]. It is important to examine these because they affect the cell performance.

2.5 SOFC modelling

Numerical modelling and simulation have become a useful tool in research and development in various engineering fields, one of them being fuel cells. Fuel cell modelling is complicated due to several interacting physical properties, such as multi-component gas flow with heat and mass transfer, electrochemical- and reforming reactions [27]. SOFC modelling at macroscopic level is often based on the Finite Element Method (FEM) or the Finite Volume Method (FVM). Examples of commercial software are FLUENT and STAR-CD, based on FVM, and COMSOL Multiphysics, based on FEM. Through computational modelling, the output can provide details of the processes, such as the fuel cell species distribution, flow patterns, current density, temperature distribution and pressure drop etc [2]. The decision to use COMSOL Multiphysics in

this thesis is because it connects different physical properties and solves the equations for these simultaneously. Two more advantages are the possibility to modify the partial differential equation in the computational model and to integrate with MATLAB. Finally, the environment that is created for the simulation facilitates all steps in the modelling process. This makes it is easy to define the geometry, specify the physics, mesh, solve and then post-process the results [28].

Multiphysics modelling takes into account the interaction between several physical properties, which can be described as partial differential equations. A good computational design considers the physical properties and the system at both a microscale and a macroscale level. As mentioned above, various models have been developed but there is still need for improvement. Some of the limitations are the lack of material data and test data in the literature to validate the models [2]. Also, another important factor during multiphysics modelling is integration issues. The equations for momentum-, heat- and mass transport are connected to each other and further depend on temperature, concentration and electrochemical reactions. Finally, modelling and simulation for different configurations of SOFCs, such as tubular and planar, usually share rather common features except for the ohmic losses and heat generation, due to material resistivity when an electric current passes through. The differences result from the diverse structures variation in the current pathway in the porous electrodes [29].

The weakness of numerical simulation is that there is no guarantee that an exact prediction of how it actually operates can be produced. Because of the numerical approximations and arbitrary unknowns implemented in the model, there will most likely be a number of errors and inaccurate results. Still, the use of numerical modelling as a predictive tool can be validated through careful consideration of results and comparison of numerical and experimental data. In a lot of computational modelling research, where the results are obtained from numerical programs, has achieved sufficient accuracy both in comparison with other different numerical modelling approaches and with experimental data [13].

The theoretical numerical models are based on detailed relationships between transport processes and electrochemical reactions. Semi-empirical models are based on experimental data specific to the operating conditions. Both semi-empirical and theoretic numerical modelling approaches have advantages and disadvantages. The theoretical numerical approach is adjustable to operating conditions, and may be preferable when detailed studies are desired. On the other hand, this approach takes longer time to develop and it is difficult to validate due to lack of detailed data in the literature. The semi-empirical approach has already been validated to some extent, but it may not provide sufficient details and should also be modified for each new application or operating condition [2]. As fuel cell testing is expensive and time consuming, a careful simulation study before testing can lower the cost for the research [4]. Despite the fact that there are some experimental data on the operational performance and temperature distribution of SOFCs, not much experimental testing has been generated because of their high operating temperature and high cost. As a result, numerical modelling of SOFCs is necessary.

3 Mathematical modelling methodology

This study is based on Andersson's extended model of the anode-supported SOFC including internal reforming. Different global internal reforming reaction schemes are applied and compared in terms of reaction rates and effects on the transport processes to apprehend the effect of the internal reforming of methane. The two-dimensional model for a single cell is implemented in COMSOL Multiphysics, which is designed for multiscale modelling and equations for momentum-, heat- and mass transport are solved at the same time. As Andersson mentioned, the model is only two-dimensional. For this reason the connection between the electrodes and the interconnect cannot be explicitly observed here. A sketch of the modelled cell used in this study is shown in Fig. 2 in section 2.2. The dimensions for the geometry are listed in Table 1.

Table 1: Cell dimensions [1]

Part of the cell	**Size [mm]**
Cell length	100
Air channel height	1
Fuel channel height	1
Electrolyte height	0,002
Cathode height	0,005
Anode height	0,05
Interconnect height	0,05

3.1 Model specifications

Below is a list of specifications. The full descriptions of the specification are given later on in the text.

- The Knudsen diffusion term is neglected.
- The entrance length for a fully developed flow profile is neglected.
- The Nusselt number is constant.
- The thermal conductivity and heat capacity are temperature independent for the solid parts in the temperature range used in this study.
- An average current density is constant.
- The gas phase appears in the electrodes, the fuel and air channels. The solid phase appears in the electrodes, the interconnects and the electrolyte.
- The temperature distribution is calculated separately for the gas and solid phases.
- The effect of electrochemical reactions on the momentum transport is included through the gas velocity effect.
- The electrochemical reactions are specified as interface conditions and not as source terms in the electrodes.
- The enthalpy and entropy changes due to chemical reactions are defined at a constant temperature.

3.2 Governing equations

3.2.1 Mass transport

To represent the mass transport for the gases within the cell, the Maxwell-Stefan equation for mass diffusion and convection is used. As mentioned before, the Maxwell-Stefan equation is a simplified equation of the Dusty Gas Model. The Knudsen term is neglected because the collision between the gas molecules and the porous medium are not considered. The Maxwell-Stefan equation is defined for the electrodes, the fuel and air channels, as below:

$$\nabla\left(-\rho \cdot w_i \sum \overline{D}_{ij} \cdot \nabla x_j + \left(x_j - w_j\right) \cdot \frac{\nabla p}{p} \cdot u - D_i^T \cdot \frac{\nabla T}{T}\right) + \rho \cdot u \cdot \nabla w_j = S_i \tag{15}$$

$$x_j = \frac{w_j}{M_j} \cdot M \tag{16}$$

$$\sum_{i=1}^{n} w_i = 1 \tag{17}$$

where w is the mass fraction, D_{ij} the Maxwell-Stefan binary diffusion coefficient, x the mole fraction, D_i^T the thermal diffusion coefficient and S_i the source term. S_i is, in this case, zero because the electrochemical reactions are assumed to take place at the interfaces between the electrolyte and electrodes. Therefore, they are defined as an interface condition and not as a source term. The diffusion coefficient in the electrodes is calculated:

$$D_{ij,por} = \frac{D_{ij} \cdot \varepsilon_p}{t} \tag{18}$$

where t is the tortuosity. Moreover, D_{ij} is calculated:

$$D_{ij} = \frac{2.66 \cdot 10^{-8} \cdot T^{3/2}}{p \cdot {M_{ij}}^{1/2} \cdot {l_{ij}}^2 \cdot \Omega_D} \tag{19}$$

$$\Omega_D = \frac{A}{\left(\frac{k' \cdot T}{e_{ij}}\right)^B} + \frac{C}{exp\left(D \cdot \frac{k' \cdot T}{e_{ij}}\right)} + \frac{E}{exp\left(F \cdot \frac{k' \cdot T}{e_{ij}}\right)} + \frac{G}{exp\left(H \cdot \frac{k' \cdot T}{e_{ij}}\right)} \tag{20}$$

$$M_{ij} = \frac{2}{\frac{1}{M_i} + \frac{1}{M_j}} \tag{21}$$

$$l_{ij} = \frac{l_i + l_j}{2} \tag{22}$$

$$e_{ij} = \sqrt{e_i + e_j} \tag{23}$$

where $\Omega_D$is the diffusion collision integral, M_{ij} the average molecular weight, l_{ij} the average characteristic length, e_{ij} the average characteristic Lennard-Jones energy and k' Boltzmann's constant. A, B, C, D, E, F, G and H are constants as in [1].

3.2.2 Heat transport

First of all, it should be mentioned that the temperature distribution is calculated separately for the gas and the solid phases. The general heat conduction equation is used to calculate the temperature distribution for the solid medium:

$$\nabla(-k_s \cdot \nabla T_s) = Q_s \tag{24}$$

where k_s is thermal conductivity for the solid media, T_s the temperature in the solid phase and Q_s the heat source. The temperature for the gas phase is calculated:

$$\nabla\left(-k_g \cdot \nabla T_g\right) = Q_g - \rho_g \cdot c_{p,g} \cdot u \cdot \nabla T_g \tag{25}$$

where T_g is the gas temperature, $c_{p,g}$ the heat capacity and Q_g the heat transfer in the gas phase. The heat transfer in the gas phase is defined as:

$$Q_g = h_v \cdot \left(T_g - T_s\right) \tag{26}$$

where h_v is the volume heat transfer coefficient. The heat capacity for each species is calculated as:

$$c_{p,i}(T) = \sum_{k=1}^{7} a_k \cdot \left(\frac{T}{1000}\right)^k \tag{27}$$

where a_k is the species dependent parameter and k is the number of species dependent parameters. After the specific heat capacity for each species, the heat capacity for the gas mixture is then calculated as:

$$c_{p,mixture} = \sum x_i \cdot c_{p,i} \tag{28}$$

The gas thermal conductivity for each species in the gas phase is calculated as:

$$k_{g,i}(T) = 0.01 \cdot \sum_{k=1}^{7} c_k \cdot \left(\frac{T}{1000}\right)^k \tag{29}$$

where c_k is the species dependent parameter. Further, the thermal conductivity for the gas mixture is then evaluated as:

$$k_{g,mixture} = \sum x_i \cdot k_{g,i} \tag{30}$$

3.2.3 Momentum transport

The Darcy-Brinkman equation is used to solve the gas flow in the gas phase:

$$\left(\frac{\mu}{\kappa}+\rho\cdot\nabla u\right)\cdot u-\nabla\left[-p+\frac{1}{\varepsilon_p}\cdot\{\boldsymbol{T}-(\lambda-\kappa_{dv})\cdot(\nabla u)\}\right]=\boldsymbol{F} \tag{31}$$

where μ is the dynamic viscosity, κ the permeability of the porous medium, ε_p the porosity, $\boldsymbol{T}$ the viscous stress tensor and $\boldsymbol{F}$ the volume force vector. λ is the second viscosity and for gases, is normally set to $\lambda=-2/3\cdot\mu$. κ_{dv} is the deviation from the thermodynamic equilibrium and is by default set to zero. The Darcy-Brinkman equation is converted into the Darcy equation when the Darcy number $Da\to 0$ and into Navier-Stokes equation when $\kappa\to\infty$ and $\varepsilon_p=1$. The equation for continuity in the fuel and air channels is calculated:

$$\nabla u=0 \tag{32}$$

The density for the gases involved is calculated:

$$\rho_{mixture}=\frac{p\cdot\sum x_i\cdot M_i}{R\cdot T} \tag{33}$$

The dynamic viscosity for each participating species in the gas phase is calculated:

$$\mu_i=\sum_{k=1}^{7}b_k\cdot\left(\frac{T}{1000}\right)^k \tag{34}$$

where b_k is the species dependent parameter and k is the number of species dependent parameters in the viscosity equation. The dynamic viscosity for the gas mixtures is calculated:

$$\mu_{mixture}=\sum x_i\cdot\mu_i \tag{35}$$

3.3 Interface and boundary conditions

3.3.1 Mass transport

The boundary conditions for the mass transport equation are defined at the gas channel inlet and the boundaries. The convective flux for the gas channel is defined as:

$$n\cdot\left(-\rho\cdot w_i\cdot\sum D_{ij}\left(\nabla x_j+(x_j-w_j)\cdot\frac{\nabla p}{p}\right)-D^T\cdot\frac{\nabla T}{T}\right)=0 \tag{36}$$

The flow from the electrodes to the electrolyte is defined as flux:

$$-n\cdot N=n_0 \tag{37}$$

$$N=-\rho\cdot w_i\cdot\sum D_{ij}\cdot\left(\nabla x_j+(x_j-w_j)\cdot\frac{\nabla p}{p}\right)+D^T\cdot\frac{\nabla T}{T}+\rho\cdot w_i\cdot u \tag{38}$$

where n is the normal vector to the boundary. Further, for the inlet the mass flux n_0 is defined as:

$$n_0 = \frac{-i \cdot M_i}{n_e \cdot F} \tag{39}$$

where i is the current density, n_e the number of electrons transferred per reaction and F the Faraday constant.

3.3.2 Heat transport

At the inlet of the gas channels, the gas temperature is defined by the operating conditions and the outlet is defined as a convective flux:

$$-n \cdot \left(-k_g \cdot \nabla T_g\right) = 0 \tag{40}$$

Because it is assumed that the cell is surrounded by cells with the same temperature, the boundaries at the top and bottom are defined as symmetry. The heat flux at the interconnect/gas channel and gas channel/electrode interfaces are defined as:

$$-n \cdot (-k_s \cdot \nabla T_s) = q_s \tag{41}$$

$$q_s = h_{s,g,ch} \cdot \left(T_s - T_g\right) \tag{42}$$

$$q_g = -q_s \tag{43}$$

$$h_{s,g,ch} = \frac{Nu \cdot k_g}{d_c} \tag{44}$$

where T_s and T_g are the temperature for the solid and gas phase respectively, similarly for the heat flux q, and $h_{s,g,ch}$ the heat transfer coefficient between the solid and the gas phase. The Nusselt Nu number is calculated to a constant value of 4.094, which is based on a rectangular duct for fully developed flow. The heat flux is specified at two channel walls opposite each other: one between the interconnect and the gas channel, and the other between the electrode and the gas channel. Further, heat is generated due to electrochemical reactions and polarization losses at the electrode/electrolyte interfaces, which are defined as:

$$-n \cdot (-k \cdot \nabla T) = q_0 \tag{45}$$

$$q_0 = q_r + q_{losses} = -i \cdot \left(\frac{T \cdot \Delta S_r}{n_e \cdot F} + \eta_{act,e} + \eta_{conc,e}\right) \tag{46}$$

$$\eta_{conc,e} = \frac{R \cdot T}{n_{e,a} \cdot F} \cdot ln\left(\frac{p_{H_2O,TPB} \cdot p_{H_2,b}}{p_{H_2,b} \cdot p_{H_2O,TPB}}\right) + \frac{R \cdot T}{n_{e,c} \cdot F} \cdot ln\left(\frac{p_{O_2,b}}{p_{O_2,TPB}}\right) \tag{47}$$

$$\eta_{act,e} = \frac{2 \cdot R \cdot T}{n_e \cdot F} \cdot sinh^{-1}\left(\frac{i_e}{2 \cdot i_{0,e}}\right) \tag{48}$$

where q_0 is the generated heat (q_r is due to enthalpy change and q_{losses} due to the potential losses within the cell), $p_{i,TPB}$ is the partial pressure at the TPB and $p_{i,b}$ at the boundary between

the gas channel and electrode. $\eta_{act,e}$ and $\eta_{conc,e}$ are the activation and concentration polarization respectively. Finally, i_0 is the exchange current density, which is defined as:

$$i_0 = \frac{R \cdot T}{n_e \cdot F} \cdot k_e'' \cdot exp\left(\frac{-E_e}{R \cdot T}\right) \tag{49}$$

$$i = 2 \cdot i_0 \cdot sinh\left(\frac{n_e \cdot F \cdot \eta_{act,e}}{2 \cdot R \cdot T}\right) \tag{50}$$

The activation polarization is often expressed by the Butler-Volmer equation which is shown in eq. (50).

3.3.3 Momentum transport

A laminar profile is adopted for the inlet with an average air velocity of 5.2 m/s. The entrance length for a fully developed flow profile is neglected because the channel length is 100 times bigger than its height. The outlet is defined at a pressure of 1 atm and

$$\mu(\nabla u + (\nabla u)^T) \cdot n = 0 \tag{51}$$

The interfaces for the interconnects are defined as walls, i.e. $u = 0$. The interface between the fuel and air channels and the electrodes are defined as continuous. The gas velocity effect is calculated at the interface between the electrolyte and the electrodes to include the electrochemical reactions. In reality the reactions occur at the active surface but are assumed here to occur at the interface. The gas velocity effect for cathode/electrolyte eq. (51) respectively anode/electrolyte interface eq. (52) is defined below:

$$r = -\left(\frac{i \cdot M_{O_2}}{n_{e,c} \cdot F \cdot \rho}\right) \tag{52}$$

$$r = \frac{i \cdot \left(M_{H_2O} - M_{H_2}\right)}{n_{e,a} \cdot F \cdot \rho} \tag{53}$$

where i is the current density, $n_{e,c}$ the number of electrons transferred per molecule of oxygen consumed (= 4) and $n_{e,a}$ the number of electons transferred per molecule of hydrogen consumed or water produced (= 2).

3.4 Internal reforming reactions

The consumption of fuel and the mole fraction are defined as:

$$C_{fuel} = \frac{x_{fuel,in} - x_{fuel,out}}{x_{fuel,in}} \tag{54}$$

$$x_{fuel} = x_{H_2} + x_{CO} + 4x_{CH_4} \tag{55}$$

where C_{fuel} is the consumption of fuel and x_i the mole fraction of molecule i. When internal reforming is applied, the parameters affected by the fuel compositions change needs to be

updated for the five species on the fuel side. The Darcy-Brinkman equation is barely affected. It is only the density, thermal conductivity and heat capacity that need to be updated for each species. The source term in Maxwell-Stefan equation includes the reaction chemistry and the Maxwell-Stefan diffusion coefficient is calculated for each pair (5 species gives 10 pairs), which inserted into the multicomponent diffusivity matrix:

$$\bar{D}_{ij} = P_{ij}^{-1} - g \tag{56}$$

$$P_{ij} = \frac{w_i \cdot w_j}{g} - \bar{C}_{ij} \tag{57}$$

$$\bar{C}_{ij} = \begin{cases} \dfrac{x_i \cdot x_j}{D_{ij}} & \mathrm{i} \neq \mathrm{j} \\ -\sum_{k \neq j} \bar{C}_{ik} & \mathrm{i} = \mathrm{j} \end{cases} \tag{58}$$

$$g = \sum_{i=1}^{n-1} \cdot \left(\sum_{j=1}^{n} D_{ij} \right) \tag{59}$$

where P_{ij}^{-1} is the inverse matrix of P_{ij} and g is a scalar value that provides numerical stability. The mass source terms, where the reaction rates are included, are defined as:

$$S_{H_2} = (3r_r + r_s) \cdot M_{H_2} \tag{7}$$

$$S_{CH_4} = -r_r \cdot M_{CH_4} \tag{8}$$

$$S_{H_2O} = (-r_r - r_s) \cdot M_{H_2O} \tag{9}$$

$$S_{CO} = (r_r - r_s) \cdot M_{CO} \tag{10}$$

As previously mentioned in chap. 2.4, the equation for CO_2 can be solved separately because the sum of the mass fractions is equal to unity. The reaction rate r_r is for the catalytic steam reforming reaction and r_s for the water-gas shift reaction.

The reaction rates for the reforming reaction are evaluated by kinetic models and for the water-gas shift reaction an equilibrium approach is applied. The two reaction kinetics applied here are from [23]. A general expression can be represented [3]:

$$r_r = k_r \cdot p_{CH_4}^m \cdot p_{H_2O}^n \cdot exp\left(-\frac{E_a}{R \cdot T}\right) \tag{60}$$

where k_r is the reaction rate constant for the steam reforming reaction, p the partial pressure, E_a the activation energy, m and n are constants. The pre-exponential factors in the reforming rate equation depend strongly on the properties of the anode material. In the literature the m-value ranges from 0.85 to 1.4, and the n-value from -1.25 to 0.8 [4, 22, 24]. For realistic results, experimental data need to be compared to the model but it is very expensive and difficult with testing. In this study, both Achenbach & Riensche [21] (eq. (61)) together with Leinfelder [26] (eq. (62)) models will be investigated. Here the reaction rate equation for Ahmed & Foger is also shown in eq. (63) because it is often cited in the literature, but it is not modelled in this study.

$$r_{r,AchRie} = 4274 \cdot p_{CH_4} \cdot exp\left(\frac{-82000}{R \cdot T_s}\right) \cdot SA \tag{61}$$

$$r_{r,Lei} = 30.8 \cdot 10^{10} \cdot p_{CH_4} \cdot p_{H_2O} \cdot exp\left(\frac{-205000}{R \cdot T_s}\right) \cdot SA \tag{62}$$

$$r_{r,AhFo} = 8542 \cdot p_{CH_4}^{0.85} \cdot p_{H_2O}^{-0.35} \cdot exp\left(\frac{-95000}{R \cdot T_s}\right) \cdot SA \tag{63}$$

where p is the partial pressure for CH_4 respective H_2O and T_s the solid phase temperature. SA is the surface area ratio. The units for all the steam reforming reaction rate equations are mol/(s·m^3). It is noticeable that Leinfelder found a positive reaction order of water and Achenbach & Riensche [21] found a reaction order of zero. Achenbach & Riensche [21] applied a 14 mm thick nickel cermet semi-disk consisting of 20 wt.% Ni and 80 wt.% ZrO_2. The total surface area was $3.86 \cdot 10^{-4}$ m^2. The temperature was varied from 700 to 940ºC and the system pressure 1.1 to 2.8 bar. Leinfelder [26] applied a 50 μm thick anode built up by two layers with 64 wt.% Ni and 36 wt.% YSZ and 89 wt.% Ni and 11 wt.% YSZ, respectively. The surface area for the anode was $2.5 \cdot 10^{-3}$ m^2. The test was conducted for the temperatures of 840 to 920ºC and at a pressure of 1 bar. The surface area ratio is varied between 1000-100000 m2/m3.

For the water-gas shift reaction, which is considered to be at equilibrium in the fuel channel, can be defined as [17]

$$r_s = k_s \cdot p_{CO} \cdot \left(1 - \frac{p_{CO_2} \cdot p_{H_2}}{K_{e,s} \cdot p_{CO} \cdot P_{H_2O}}\right) \tag{64}$$

$$K_{e,s} = exp\left(\frac{4276}{T} - 3.961\right) \tag{65}$$

where k_s is the reaction rate constant and $K_{e,s}$ the equilibrium constant for the water-gas shift reaction. The unit for the water-gas shift reaction rate is mol/(s·m^3). The heat generation or consumption due to the reforming reaction, are defined as source terms. The enthalpy change can be found in Table 2:

$$Q_{int\ ref} = \sum_i r_i \cdot \Delta h_{reac,i} \tag{66}$$

Table 2: Enthalpy change for the reforming reactions [8]

Reaction	**Enthalpy change (at 1000K) [kJ/mol]**
Steam reforming	226
Water-gas shift	-35

The conditions of the SOFC internal reforming process vary along the channel length of the cell which implicates for modelling purposes that a differential treatment of the problem is necessary [21]. In order to broaden the operational range for steam reforming, catalysts are modified by the addition of basic compounds, e.g. alkali and alkaline earth metals for suppression of carbon formation by improving steam retention [25].

4 Results

Data for the materials properties occurring in the literature is listed in Table 3 [1].

Table 3: Material data [1]

Anode thermal conductivity, $k_{s,a}$	11	W/m/K
Cathode thermal conductivity, $k_{s,c}$	6	W/m/K
Electrolyte thermal conductivity, $k_{s,el}$	2.7	W/m/K
Interconnect thermal conductivity, $k_{s,int}$	20	W/m/K
Anode heat capacity, $c_{p,a}$	450	J/kg/K
Cathode heat capacity, $c_{p,c}$	430	J/kg/K
Electrolyte heat capacity, $c_{p,el}$	470	J/kg/K
Interconnect heat capacity, $c_{p,int}$	550	J/kg/K
Anode solid density, ρ_a	3310	kg/m^3
Cathode solid density, ρ_c	3030	kg/m^3
Electrolyte solid density, ρ_{el}	5160	kg/m^3
Interconnect solid density, ρ_{int}	3030	kg/m^3
Permeability, κ_e	$1.76 \cdot 10^{11}$	m^2
Porosity, ε_e	0.5	-
Electrode particle diameter, d_p	1	μm
Tortuosity, t	5	-

4.1 Base conditions

The inlet temperature is specified to be 1100 K both for the air and the fuel channels, and the surface area ratio 1000 m^2/m^3. The average cell current density is specified to 0.3 A/cm^2 and the fuel utilization to 80%. The oxygen surplus factor is set to 4, which means that the oxygen utilization is 20%. The fuel gas inlet conditions, which are defined according to IEA [1], are specified as:

$$x_{H_2} = 0.2626 \quad (67)$$

$$x_{CH_4} = 0.171 \quad (68)$$

$$x_{CO} = 0.0294 \quad (69)$$

$$x_{H_2O} = 0.4934 \quad (70)$$

$$x_{CO_2} = 0.0436 \quad (71)$$

The model has parallel flow and the flow direction is set to be from left to right for air and fuel channels as well as the anode and the cathode. It should be explicitly mentioned that the length of the cell is 100 times longer than the height of the air or fuel channel.

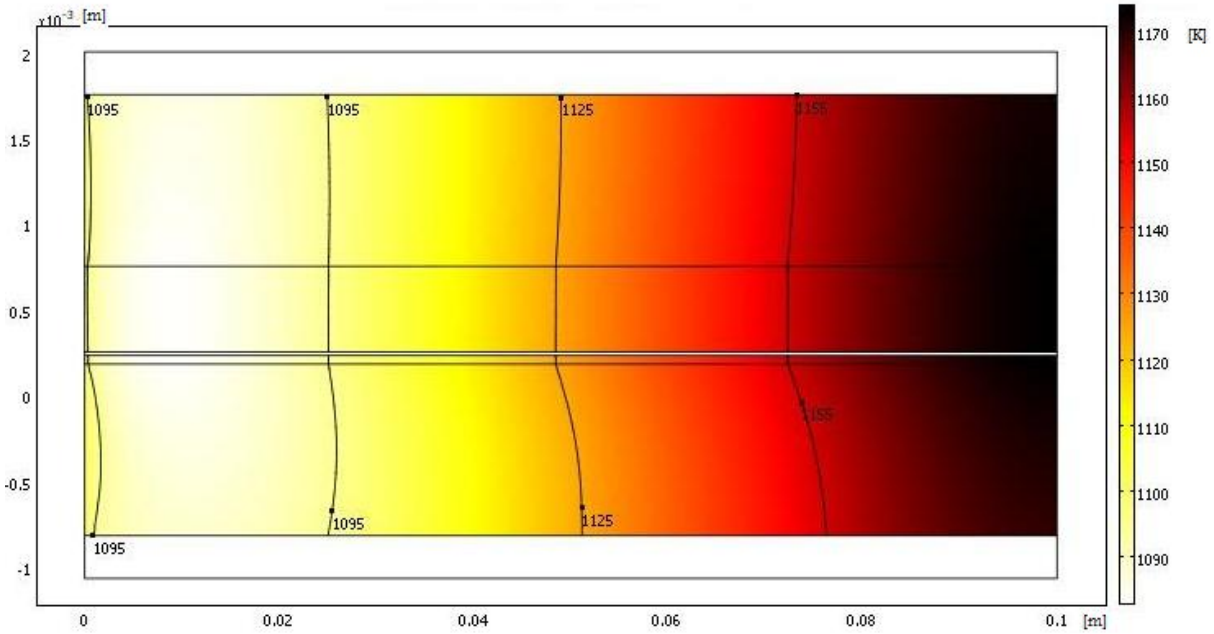

Figure 3: The temperature distribution [K] for Achenbach & Riensche's model.

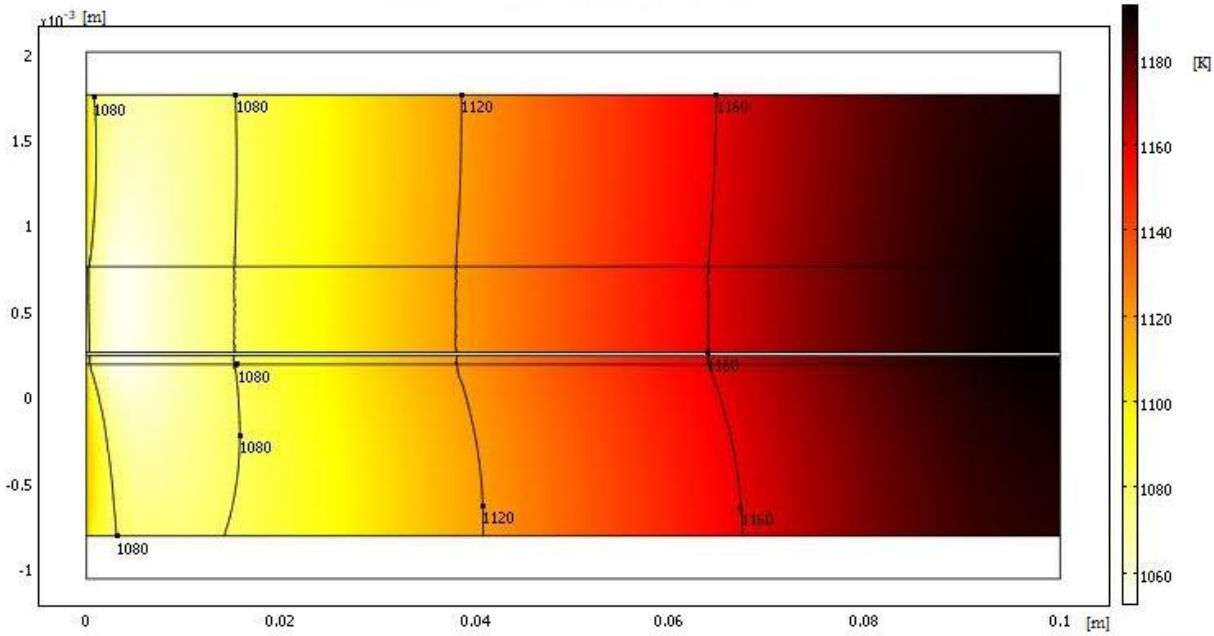

Figure 4: The temperature distribution [K] for Leinfelder's model.

The gas phase temperature in the cell is plotted in Figs. 3 and 4 for Achenbach & Riensche's model and Leinfelder's model respectively. There is a decrease in temperature a short distance from the inlet for both the fuel and air channels. In the air and fuel channels this is due to the steam reforming reaction, which decreases the temperature when the methane is reformed to hydrogen and carbon monoxide. The temperature on the air side is lower due to a higher air flow rate. The decrease in temperature close to the inlet is 10 K for Achenbach & Riensche's model and 45 K for Leinfelder's model respectively. The decrease in temperature is higher for Leinfelder's model due to a faster steam reforming reaction rate as shown in Fig. 12 and discussed in the conclusions.

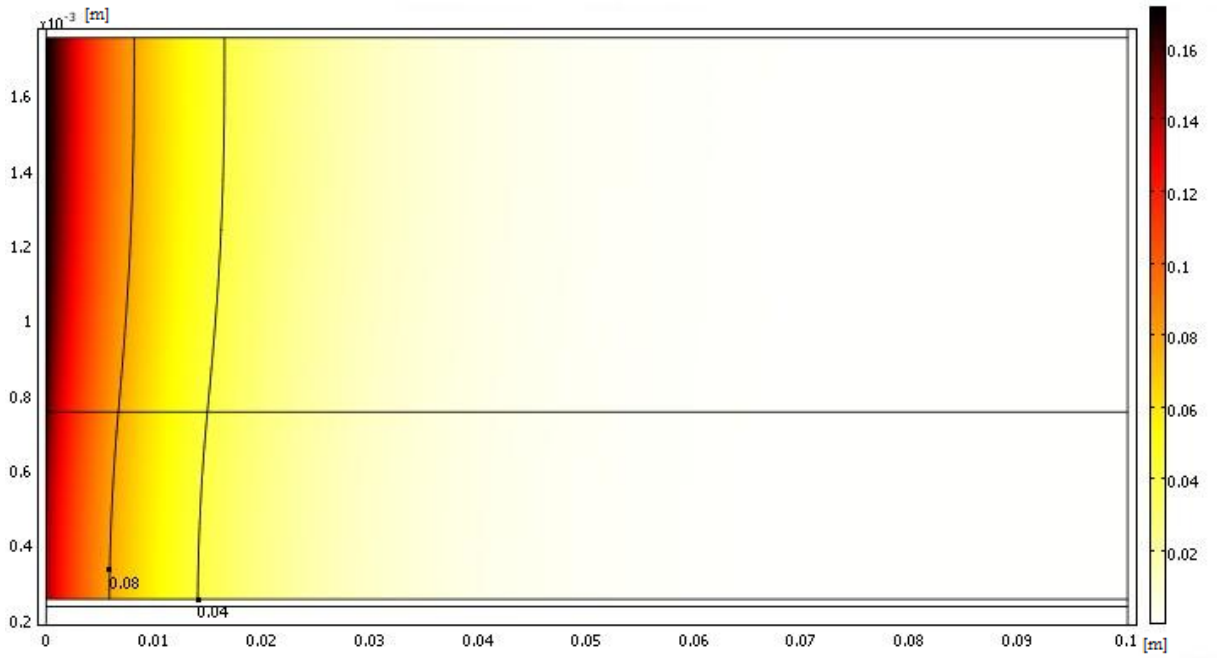

Figure 5: The mole fraction of methane in the anode and fuel channels for Achenbach & Riensche's model.

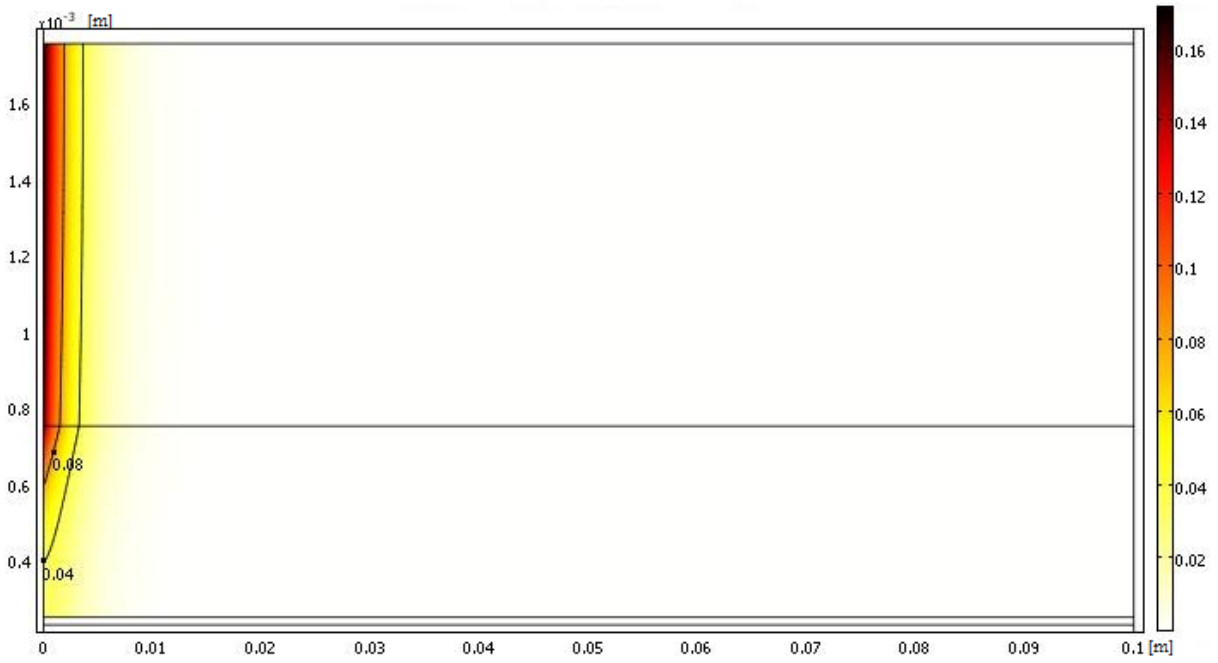

Figure 6: The mole fraction of methane in the anode and fuel channels for Leinfelder's model.

The mole fraction distribution of methane is plotted in Figs. 5 and 6 for Achenbach & Riensche's model and Leinfelder's model respectively. The mole fraction is highest at the inlet and then gradually decreases because methane is reformed to hydrogen and carbon monoxide. The concentration difference along the y-axis is due to the fact that methane is consumed in the porous structure and subsequently methane diffuses to the porous anode from the fuel channel. The decrease in mole fraction of methane is larger for Leinfelder's model than for Achenbach & Riensche's model due to a faster steam reforming reaction rate.

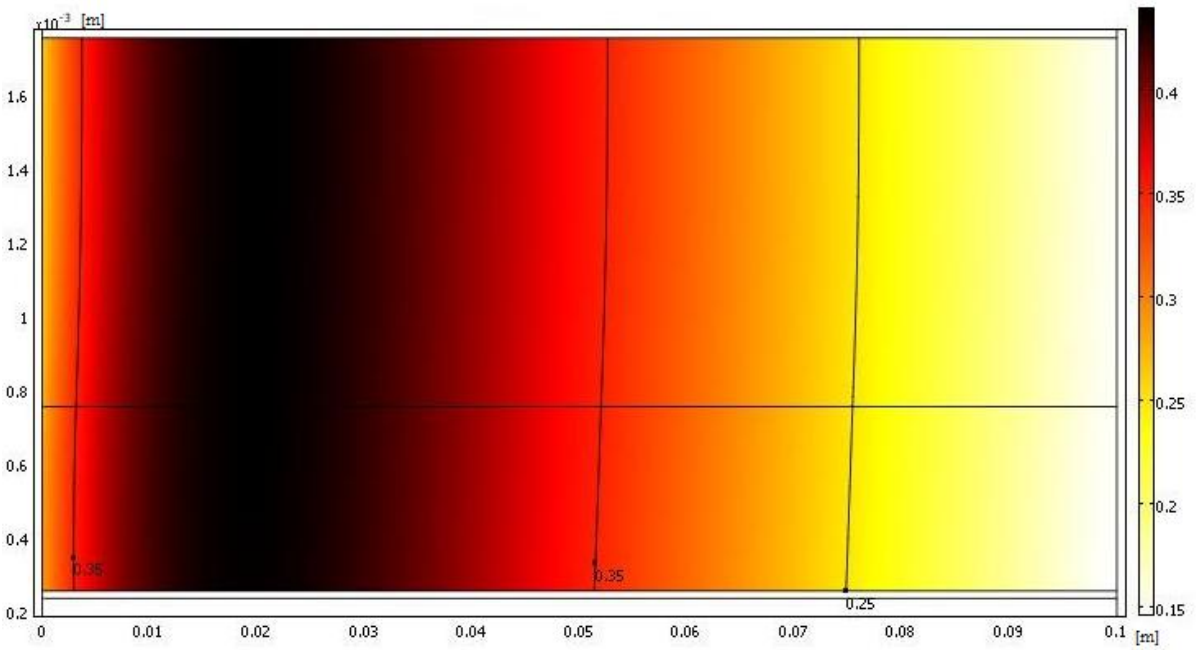

Figure 7: The mole fraction of hydrogen in the anode and fuel channels for Achenbach & Riensche's model.

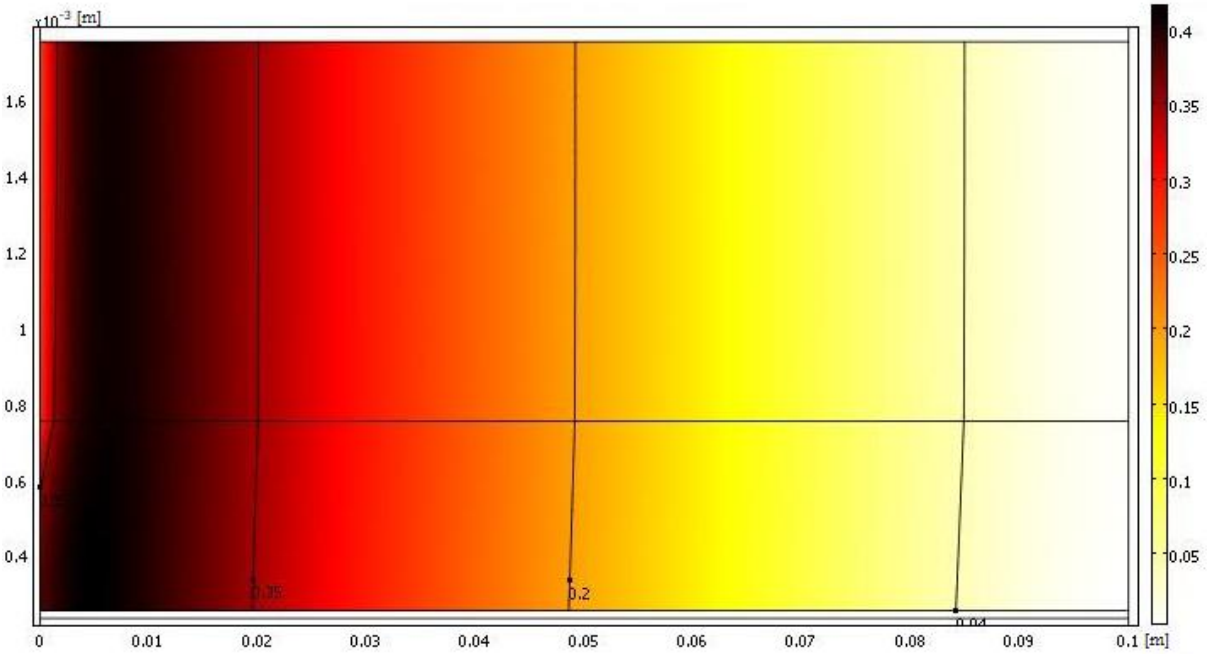

Figure 8: The mole fraction of hydrogen in the anode and fuel channels for Leinfelder's model.

The mole fraction distribution of hydrogen is plotted in Figs. 7 and 8 for Achenbach & Riensche's model and Leinfelder's model respectively. The mole fraction of hydrogen increases as methane and carbon monoxide are converted into hydrogen and the highest concentration of hydrogen is found where most methane is converted. More hydrogen is generated through the cell due to the water-gas shift reaction. Hydrogen is consumed where the electrochemical reactions occur. The highest concentration for hydrogen occurs closer to the inlet for Leinfleder's model than for Achenbach & Riensche's model due to a faster reaction rate.

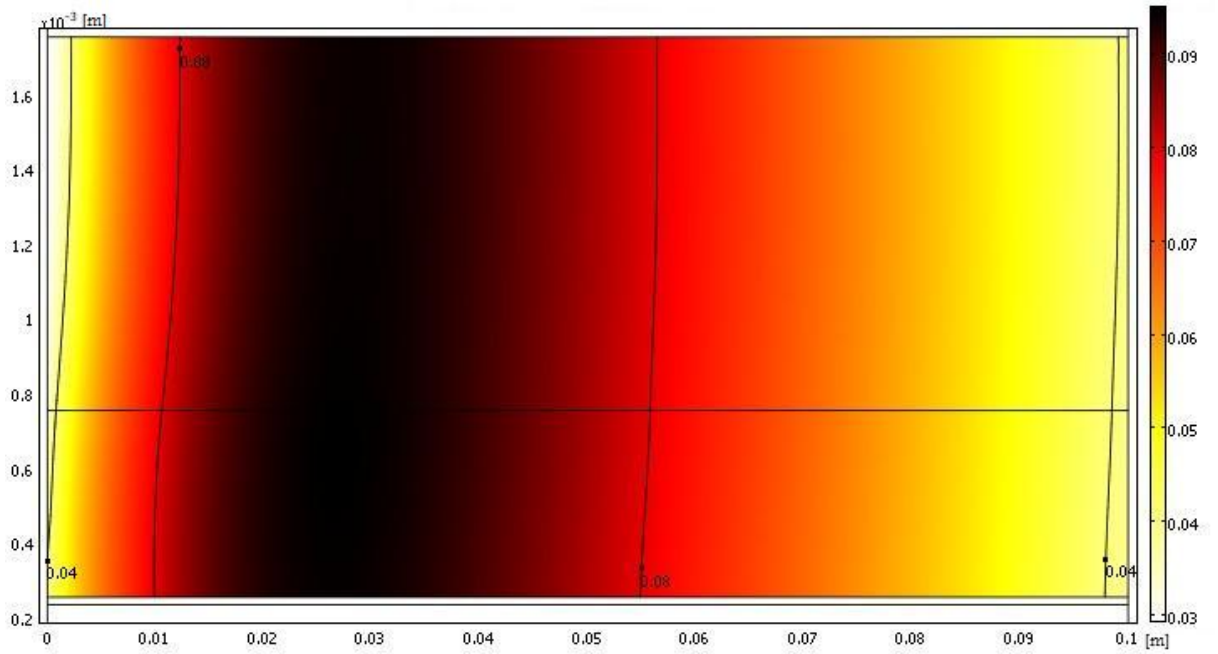

Figure 9: The mole fraction of carbon monoxide in the anode and fuel channels for Achenbach and Riensche's model.

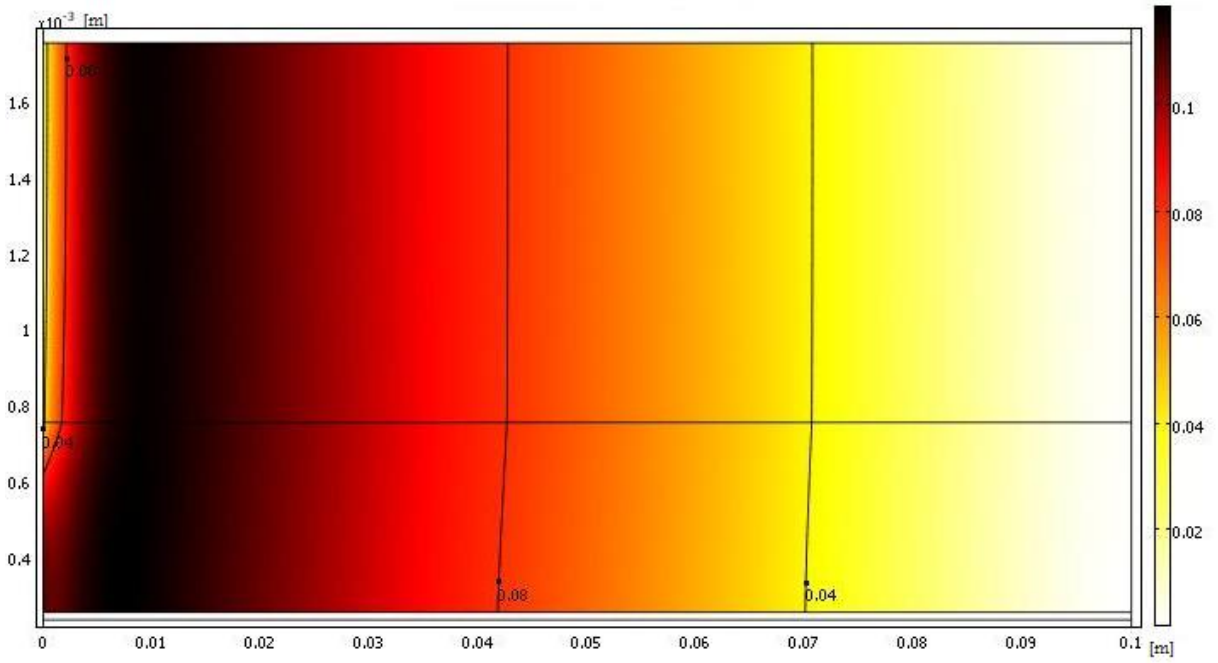

Figure 10: The mole fraction of carbon monoxide in the anode and fuel channels for Leinfelder's model.

The mole fraction distribution of carbon monoxide is plotted in Fig. 9 and 10 for Achenbach & Riensche's model and Leinfelder's model respectively. As methane is reformed, carbon monoxide is generated and further gradually converted to hydrogen and carbon dioxide. Methane reforming only takes place in the porous anode and therefore there will be a concentration difference in y-direction especially close to inlet. The highest concentration can be found when all the methane has been reformed. The concentration is higher closer to the inlet for Leinfelder's model due to the faster reaction rate and also the concentration reaches a slightly higher value.

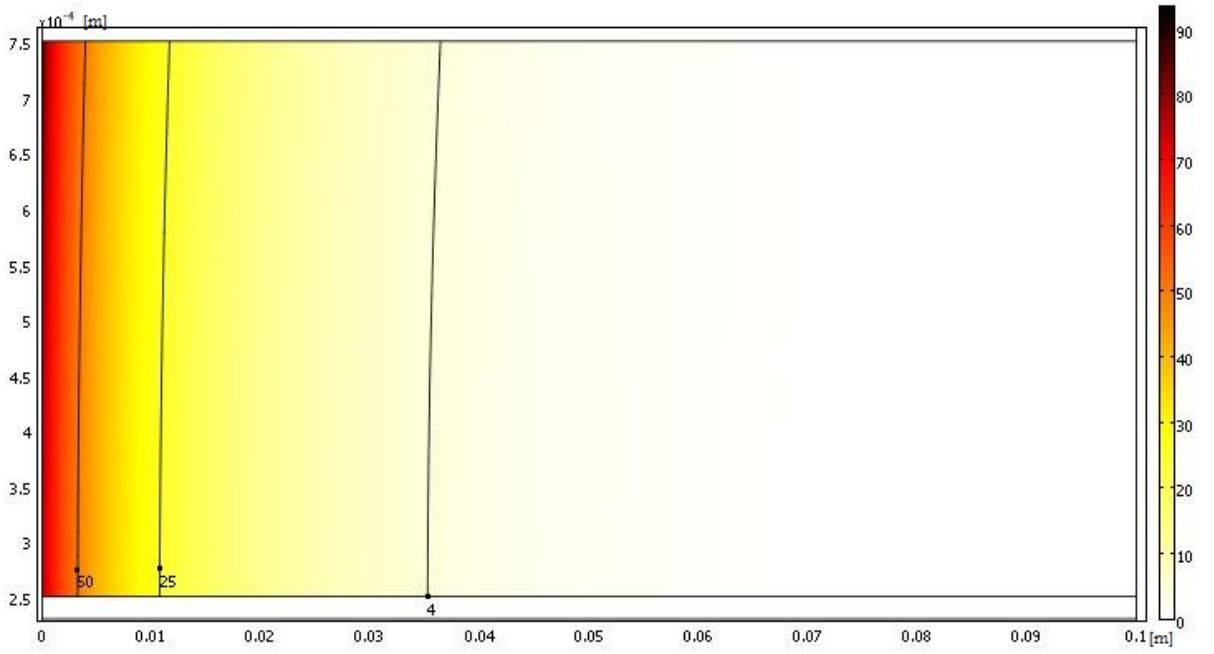

Figure 11: The reaction rate for the steam reforming reaction [mol/(s·m^3)] in the anode for Achenbach & Riensche's model.

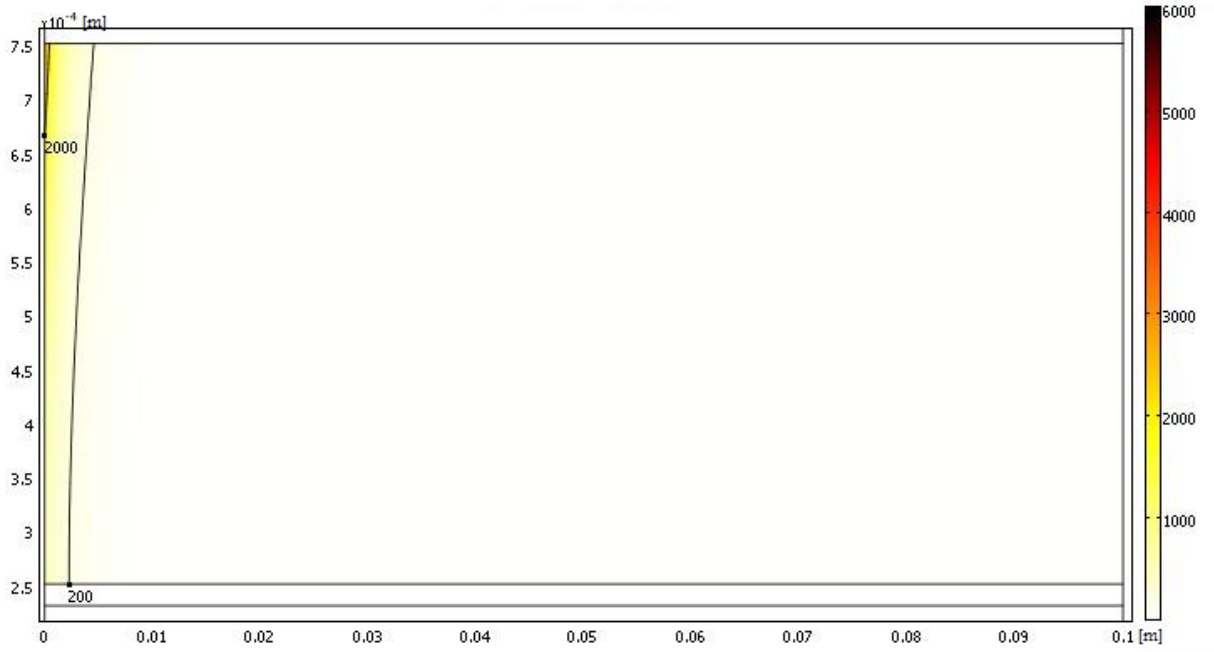

Figure 12: The reaction rate for the steam reforming reaction [mol/(s·m^3)] in the anode for Leinfelder's model.

The reaction rate for the steam reforming reaction is plotted in Figs. 11 and 12 for Achenbach & Riensche's model and Leinfelder's model respectively. The reaction rate is high where the concentration of methane is high. All of the anode depth is used for the reaction. As shown in the figures, the reaction rate for the steam reforming is much faster for Leinfelder's model than for Achenbach & Riensche's model.

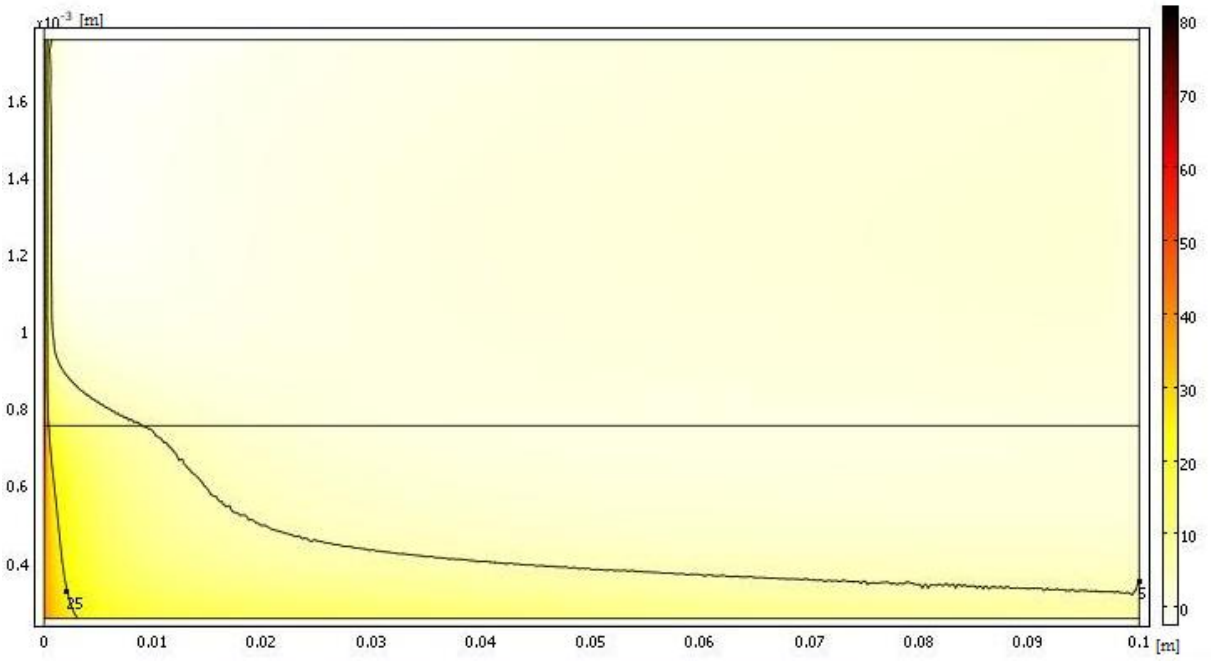

Figure 13: The reaction rate for the water-gas shift reaction [mol/(s·m^3)] in the anode and fuel channels for Achenbach & Riensche's model.

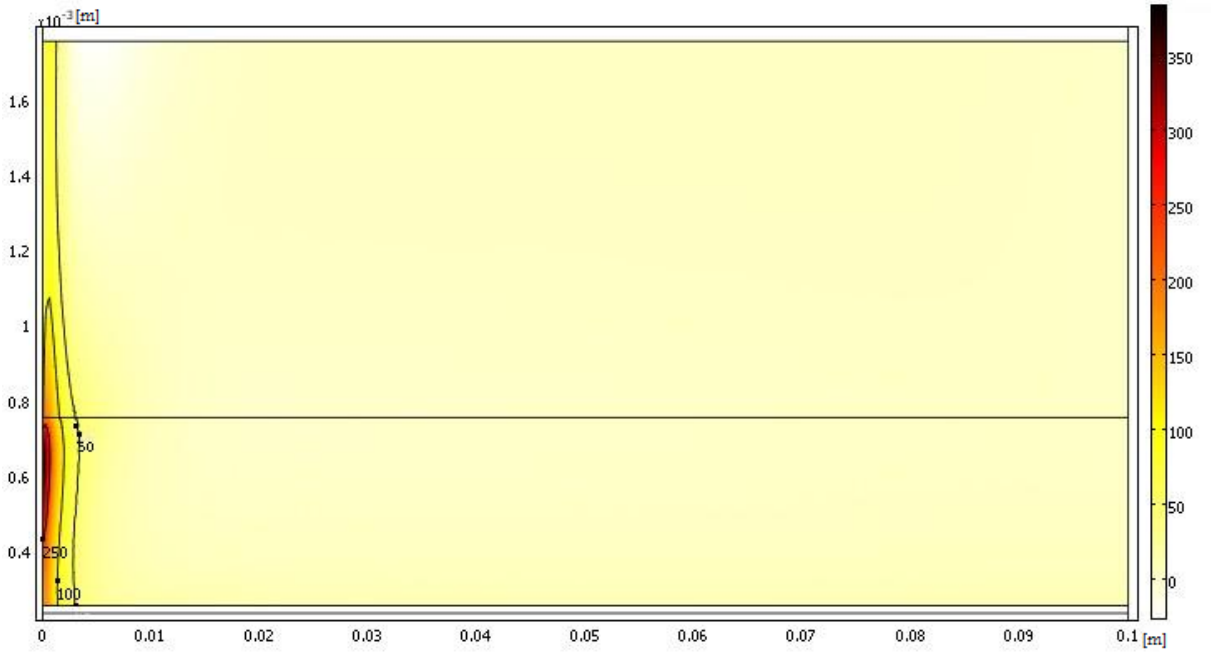

Figure 14: The reaction rate for the water-gas shift reaction [mol/(s·m^3)] in the anode and fuel channels for Leinfelder's model.

The reaction rate for the water-gas shift reaction is plotted in Figs. 13 and 14 for Achenbach & Riensche's model and Leinfelder's model respectively. The reaction rate is at the highest close to the inlet in the anode where carbon monoxide generation is high. The generation is high due to the steam reforming reaction. Furthermore, more hydrogen is produced when steam is generated. The steam is generated due to the electrochemical reaction at the TPB and this will cause the water-gas shift reaction to proceed to the right. The reaction rate for Leinfleder's model reaches a higher value due to the faster reaction rate for the steam reforming reaction.

4.2 Temperature effects

The inlet temperature is varied between 1150 K and 1050 K with an interval of 50 K for Achenbach & Riensche's model. The other parameters were kept the same as in the base case.

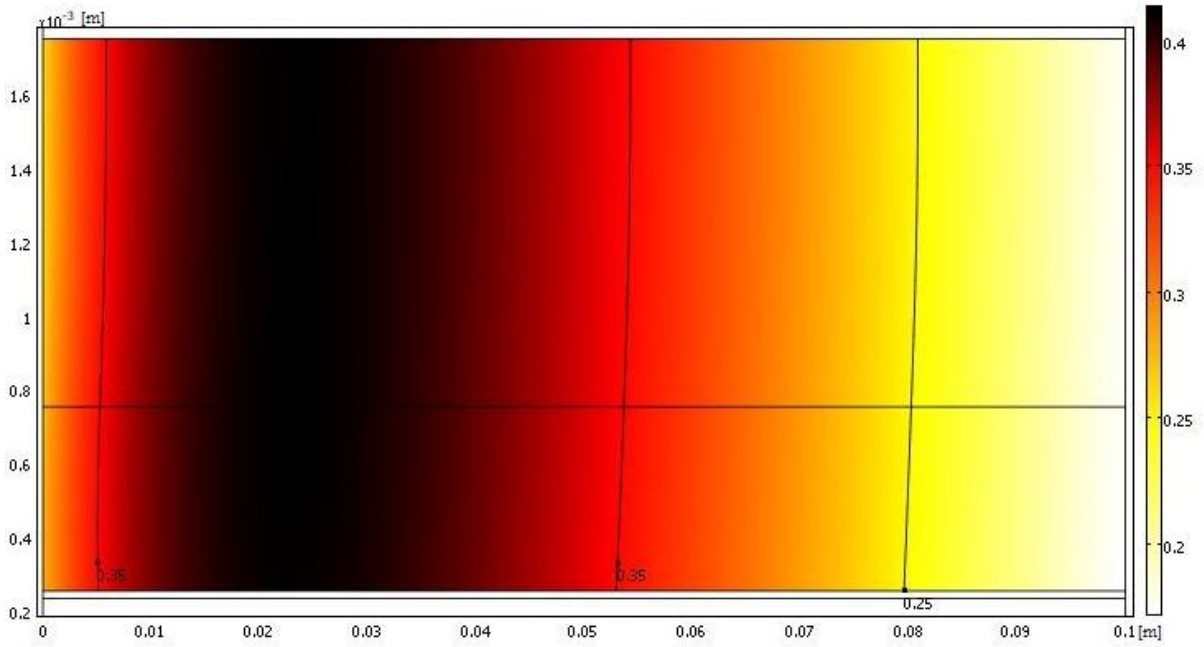

Figure 15: The mole fraction of hydrogen for Achenbach & Riensche's model at an inlet temperature of 1050 K.

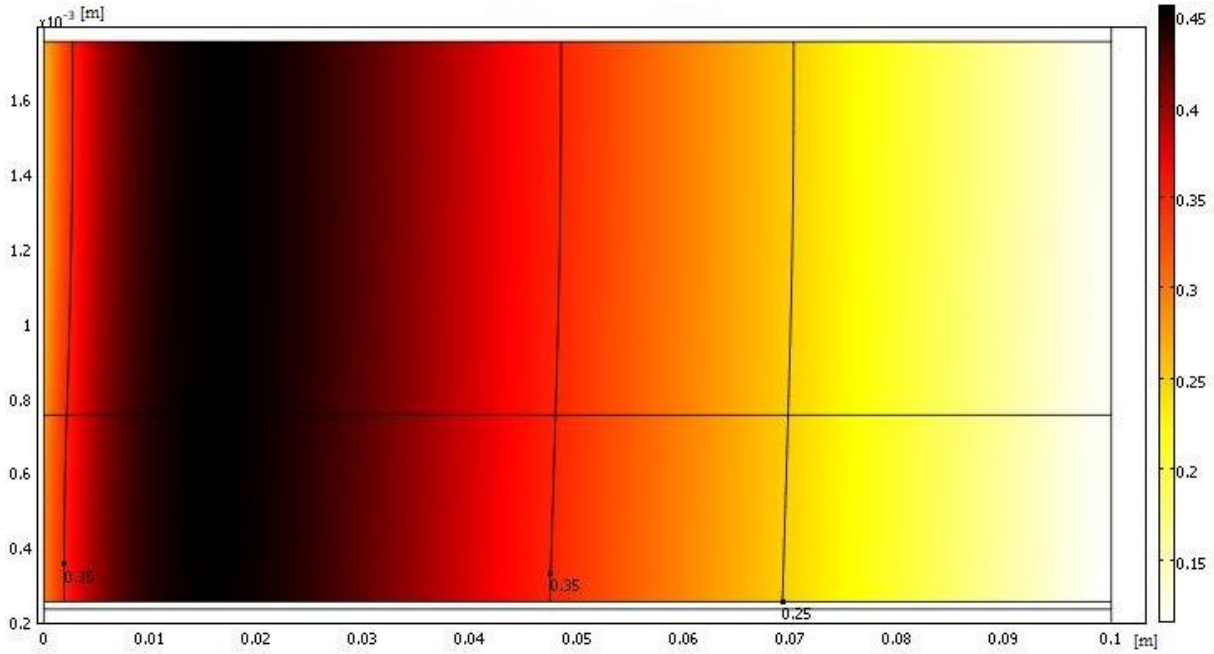

Figure 16: The mole fraction of hydrogen for Achenbach & Riensche's model at an inlet temperature of 1150 K.

The mole fraction of hydrogen in the anode and the fuel channel is plotted in Figs. 15 and 16 for Achenbach & Riensche's model. The highest value for both cases is about the same. The higher

inlet temperature produces the highest value occurring closer to the inlet. The predictions for the other mole fractions are similar to the case for hydrogen, i.e. that the maximum value is the same and that the higher inlet temperature brings the higher value closer to the inlet. Because of the similarity the profiles for the other mole fractions are not shown here in the results.

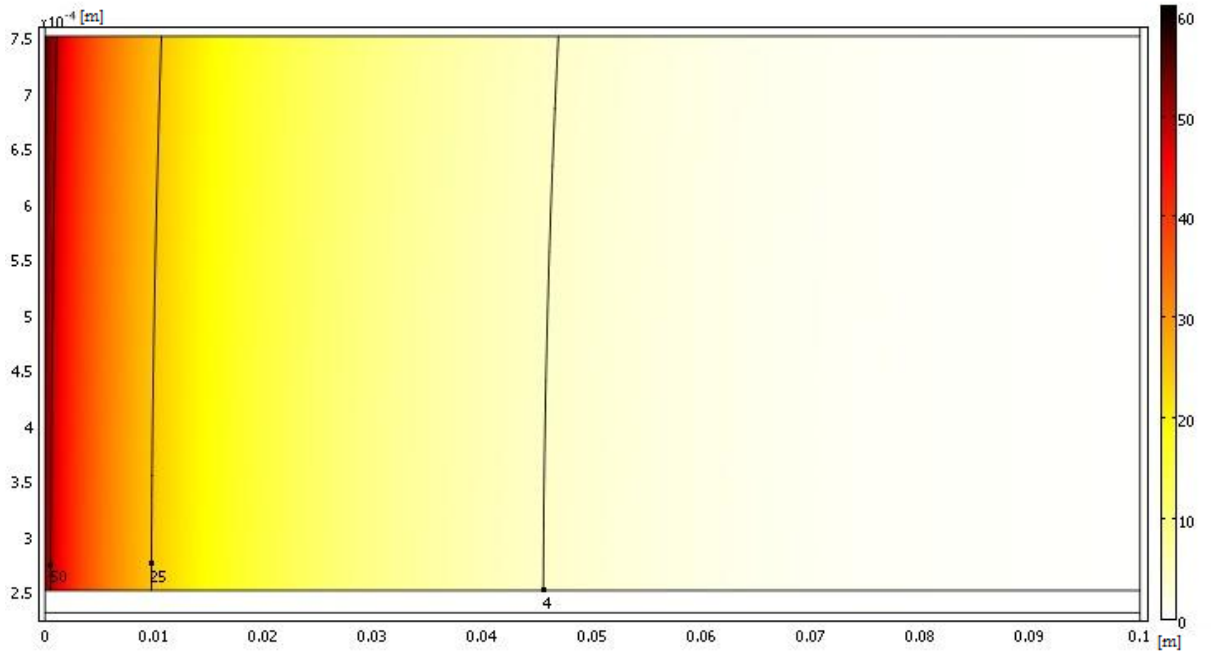

Figure 17: The reaction rate for the steam reforming reaction [mol/(s·m³)] for Achenbach & Riensche's model at an inlet temperature of 1050 K.

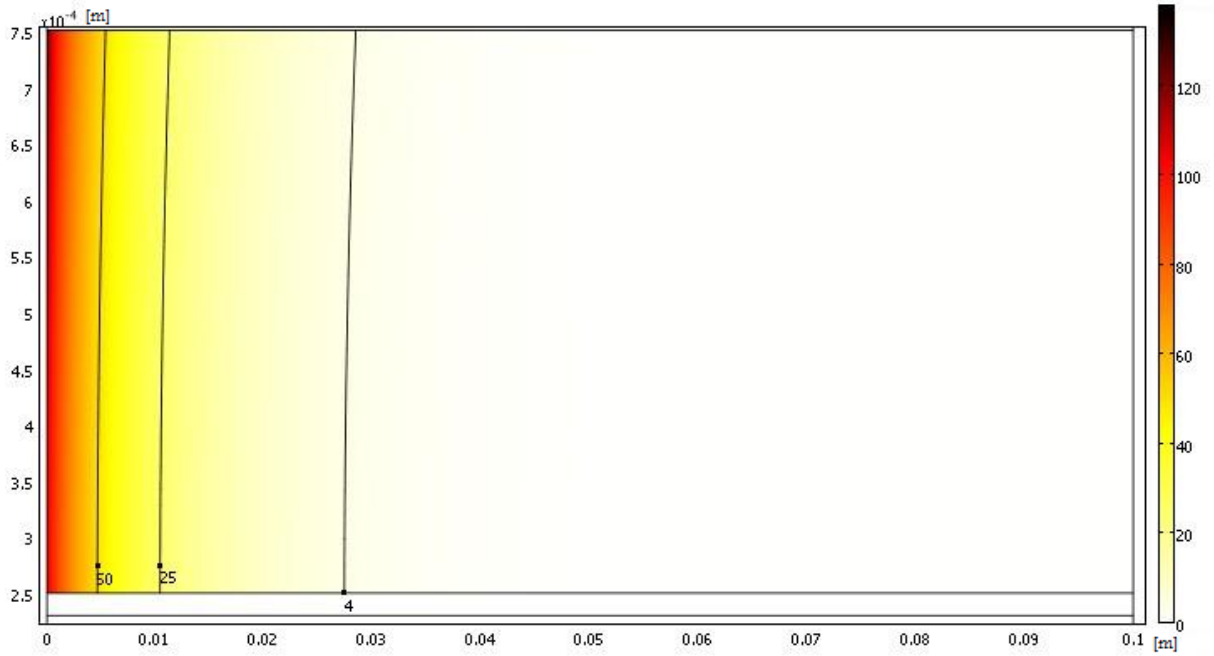

Figure 18: The reaction rate for the steam reforming reaction [mol/(s·m³)] for Achenbach & Riensche's model at an inlet temperature of 1150 K.

The reaction rate for the steam reforming reaction is plotted in Figs. 17 and 18 for Achenbach & Riensche's model. The major difference is that the maximum value is higher for the case with a higher inlet temperature. The temperature distribution for both cases shows a similar trend with a

temperature drop at about 10 K close to the inlet but this is not shown here because of the similarity.

4.3 Surface area ratio effects

The surface area ratio is varied between 1000, 50000 and 100000 m^2/m^3 for Achenbach & Riensche's model. All the other parameters are kept the same as the base case. In this section the plots shown are for the surface area ratio of 50000 and 100000 m^2/m^3.

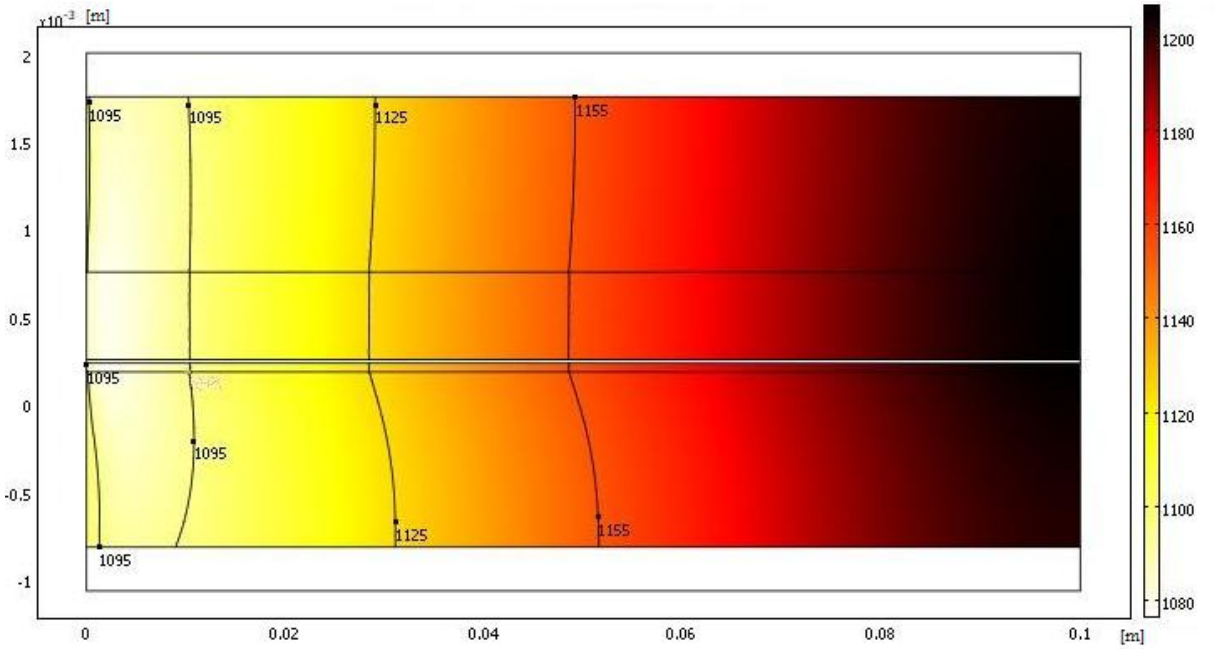

Figure 19: The temperature distribution [K] for Achenbach & Riensche's model at SA=50000 m^2/m^3.

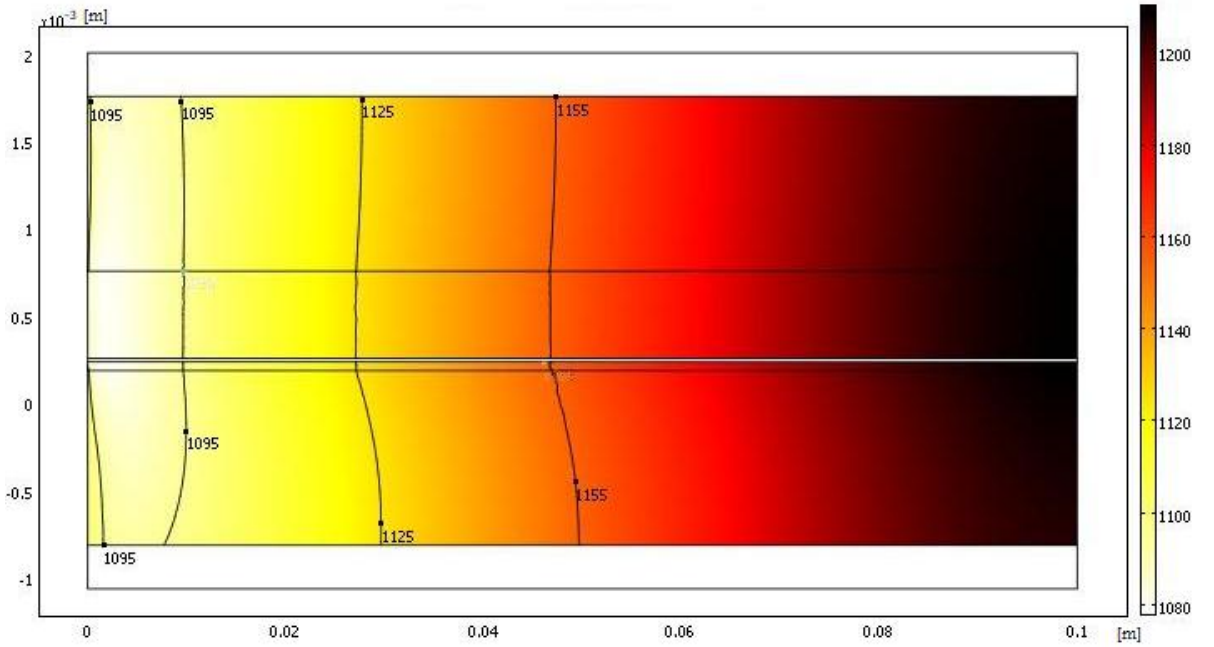

Figure 20: The temperature distribution [K] for Achenbach & Riensche's model at SA=100000 m^2/m^3.

The gas-phase temperature in the cell is plotted in Fig. 19 and 20 for Achenbach & Riensche's model. The temperature distribution is almost the same for both cases shown here. But compared to the base case the maximum and minimum temperature differs by 30 K and 10 K respectively. Each mole fraction behaves in a similar way as the specific base case for that mole fraction. By and large, the mole fractions reach the same maximum value for the different surface area ratios but occur at different distances from the inlet. A higher surface area ratio results in the maximum value occurring closer to the inlet. The plots are not shown here because of the similarity to the base case.

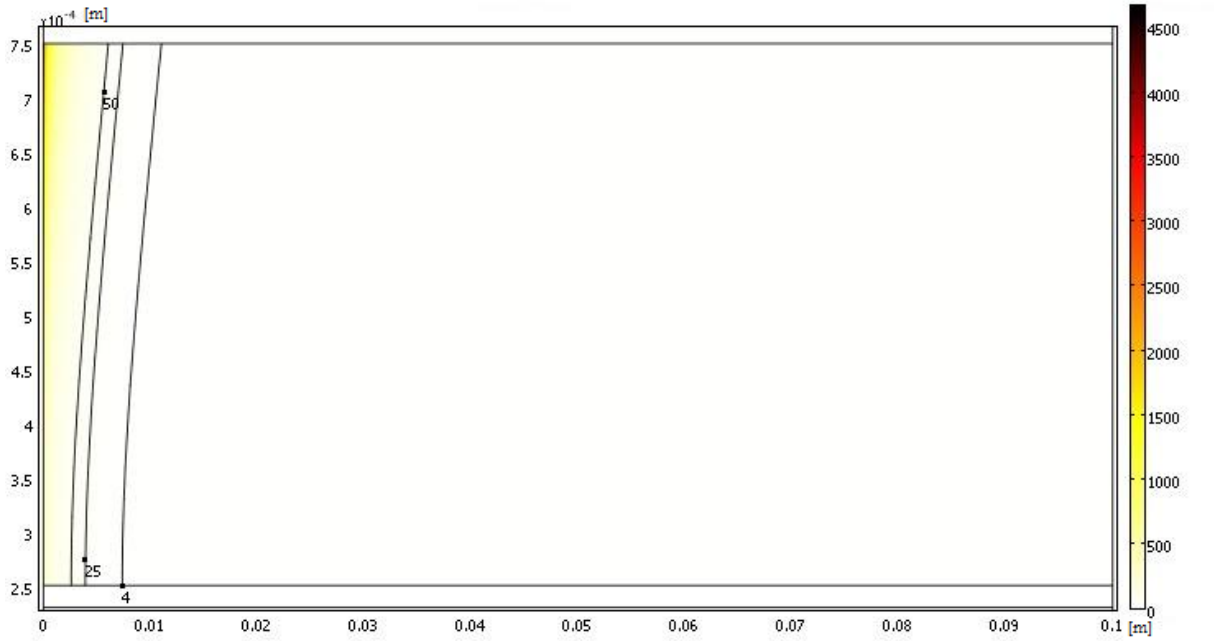

Figure 21: The reaction rate for the steam reforming reaction [mol/(s·m³)] for Achenbach & Riensche's model at SA=50000 m²/m³.

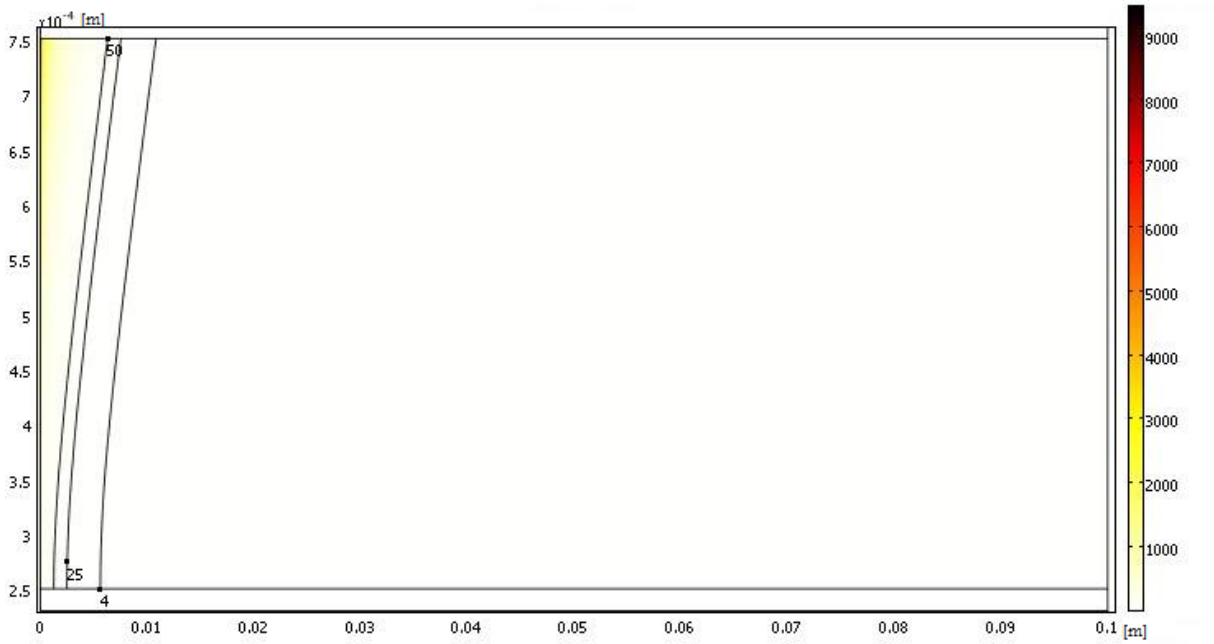

Figure 22: The reaction rate of the steam forming reaction [mol/(s·m³)] for Achenbach & Riensche's model at SA=100000 m²/m³.

The reaction rate for the steam reforming reaction is plotted in Figs. 21 and 22 for Achenbach & Riensche's model. The characteristics are similar but the maximum value is almost doubled for a doubled surface area ratio.

5 Conclusions

The purpose of this study was to further extend Andersson's finite-element-based model [1] of the anode-supported SOFC to better understand the effects of the internal reforming of methane on the transport processes. A CFD approach was implemented for the analysis and the equations for momentum-, heat- and mass transport were solved simultaneously. COMSOL Multiphysics was used to analyze the effects of two different global kinetic models by changing the steam reforming reaction only. The two different reaction rates, which were of interest here, were established through experimental work by Achenbach & Riensche [21], and Leinfelder [26]. An equilibrium equation for the reaction rate for the water-gas shift reforming reaction was used for the models. A parameter study was also investigated for the inlet temperature and surface area ratio effect.

First of all, the base case conditions for Achenbach & Riensche's model and Leinfelder's model were evaluated. The temperature decrease reaches a minimum close to the inlet for both cases. The decrease was at about 10 K for Achenbach & Riensche's model and 45 K for Leinfelder's model, which is expected because Leinfelder's model has a faster steam reforming reaction rate. The faster steam reforming reaction rate was due to that both the partial pressure for the methane and water was concluded for Leinfelder's model. Leinfelder's model also has a much higher pre-exponential value. Throughout the compared results, Leinfelder's model obtained the maximum value faster and/or a higher maximum value than Achenbach & Riensche's model did. It was revealed by that the reaction rate for Leinfelder's model was more than 60 times faster than Achenbach & Riensche's model. Furthermore, the effects of the inlet temperature change and surface area ratio change were investigated for Achenbach & Riensche's model. The inlet temperature change had a significant effect on the reaction rates in terms of the maximum value. When the inlet temperature increased from 1050 K to 1150 K, the maximum value for the steam reforming reaction rate was more than doubled. The surface area ratio had effects on the temperature distribution and the reaction rates. Temperatures increase faster for a higher surface area ratio and reach a higher maximum value. The maximum steam reforming reaction rate was almost doubled when the surface area ratio was doubled. The results were compared to the results of Andersson [1]. The results for Achenbach & Riensche's model were similar to Andersson's. The steam reforming reaction for Achenbach & Riensche was slightly faster but the steam reforming reaction rate for Leinfelder's model was much faster compared to the model used in Andersson [1]. This resulted in the same conclusions drawn from the comparison between Achenbach & Riensche's model and Leinfelder's model as between the model used in Andersson [1] and Leindfelder's model.

6 References

[1] Andersson M., SOFC Modeling Considering Mass and Heat Transfer, Fluid Flow with Internal Reforming Reactions, Licentiate Thesis, Department of Energy Sciences, Lund University, Sweden, ISSN 0282-1990, 2009

[2] Yuan J., Faghri M., Sundén B., On Heat and Mass Transfer Phenomena in PEMFC and SOFC and Modeling Approaches, Chapter 4 in Sundén B., Faghri M.(eds.), Transport Phenomena in Fuel Cells, WIT Press, UK, 2005

[3] Yang Y., Du X., Yang L., Huang Y., Xian H., Investigation of Methane Steam Reforming in Planar Porous Support of Solid Oxide Fuel Cell, Applied Thermal Engineering, 29, pp. 1106-1113, 2009

[4] Sanchez D., Chacartegui R., Munoz A., Sanchez T., On the Effect of Methane Internal Reforming in Solid Oxide Fuel Cells, Int. J. Hydrogen Energy, 33, pp. 1834-1844, 2008

[5] Janarhanan V., Deutschmann O., CFD Analysis of a Solid Oxide Fuel Cell with Internal Reforming, J. Power Sources, 162, pp. 1192-1202, 2006

[6] Hecht E., Gupta G., Zhu H., Dean A., Kee R., Maier L., Deutschmann O., Methane Reforming Kinetics within a Ni-YSZ SOFC Anode Support, Applied Catalysis A: General, 295, pp. 40-51, 2005

[7] Barry P. L., http://science.nasa.gov/headlines/y2003/images/fuelcell/sofc-brochure-new.gif, 2009-08-03

[8] Yuan J., Huang Y., Sundén B., Wang W.G., Analysis of Parameter Effects on Chemical Coupled Transport Phenomena in SOFC Anodes, Heat Mass Transfer, 45, pp. 471-484, 2009

[9] Yuan J., Ren F., Sundén B., Analysis of Chemically Reacting Transport Phenomena in an Anode Duct of Intermediate Temperature SOFCs, J. Fuel Cell Sci. Technol., 3, pp. 687-701, 2006

[10] Nam J. H., Jeon D. H., A Comprehensive Micro-scale Model for Transport and Reaction in Intermediate Temperature Solid Oxide Fuel Cells, Electrochim. Acta, 51 pp. 3446-3460, 2006

[11] Hussain M. M., Li. X., Dincer I., Mathematical Modeling of Transport Phenomena in Porous SOFC Anodes, Int. J. Thermal Sciences, 46, pp. 48-86, 2007

[12] Sundén B., "Compendia in Heat and Mass Transfer", Division of Heat Transfer, Department of Energy Sciences, Faculty of Engineering, Lund University, 2009

[13] Kackac S., Pramuanjaroenkij A., Zhou X., A Review of Numerical Modeling of Solid Oxide Fuel Cells, Int. J. Hydrogen Energy, 32, pp. 761-786, 2007

[14] Lehnert W., Meusinger J., Thom F., Modelling of Gas Transport Phenomena in SOFC Anodes, J. Power Sources, 87, pp. 57-63, 2000

[15] Yakabe H., Hishinuma M., Uratani M., Matsuzaki Y., Yasuda I., Evaluation and Modeling of Performance of Anode-Supported Solid Oxide Fuel Cell, J. Power Sources, 86, pp.423-431, 2000

[16] Suwanwarangkul R., Croiset E., Fowler M. W., Douglas P. L., Entchev E., Douglas M. A., Performance Comparison of Fick's, Dusty Gas and Stefan-Maxwell Models to Predict the Concentration Overpotential of a SOFC Anode, J. Power Sources, 122, pp. 9-18, 2003

[17] Aguiar P., Adjiman C. S., Brandon N. P., Anode-Supported Intermediate Temperature Direct Internal Reforming Solid Oxide Fuel Cell I: Model-Based Steady-State Performance, J. Power Sources, 132, pp.113-126, 2004

[18] Klein J.-M., Bultel Y., Georges S., Pons M., Modeling of a SOFC Fuelled by Methane: From Direct Reforming to Gradual Internal Reforming, Chem. Eng. Sci., 62, pp. 1636-1649, 2007

[19] Shaffer B., Brouwer J., Dynamic Model for Understanding Spatial Temperature and Species Distributions in Internal-Reforming Solid Oxide Fuel Cells, Proceedings of ASME 2009 Seventh International Fuel Cell Science, Engineering and technology Conference, New Port Beach, California, USA, 2009

[20] Damm D. L., Fedorov A.G., Local Thermal Non-Equilibrium Effects in Porous Electrodes of the Hydrogen Fueled SOFC, J. Power Sources, 159, pp. 1153-1157, 2006

[21] Achenbach E., Riensche E., Methane/Steam reforming Kinetics for Solid Oxide Fuel Cells, J. Power Sources, 52, pp. 283-288, 1994

[22] Aguiar P., Adjiman C. S., Brandon N. P., Anode-Supported Intermediate-Temperature Direct Internal Reforming Solid Oxide Fuel Cell II: Model-Based Dynamic Performance and Control, J. Power Sources, 147, pp. 136-147, 2005

[23] Janardhanan V. M., Deutschmann O., Numerical Study of Mass and Heat Transport in Solid-Oxide Fuel Cells Running on Humidified Methane, Chem. Eng. Sci., 62, pp. 5473-5486, 2007

[24] Nagel F. P., Schildhauer T. J., Biollaz S. M. A., Stucki S., Charge, Mass and Heat Transfer Interactions in Solid Oxide Fuel Cells Operated with Different Fuel Gases- A Sensitivity Analysis, J. Power Sources, 184, pp. 129-142, 2008

[25] Ahmed K., Foger K., Kinetics of Internal Steam Reforming of Methane on Ni/YSZ-based Anodes for Solid Oxide Fuel Cells, Catalysis Today, 63, pp. 479-487, 2000

[26] Leinfelder R., Reaktionskinetische Untersuchungen zur Methan-Dampf-Reformierung und Shift-Reaktion an Anoden Oxidkeramischer Brennstoffzellen, Doctoral Thesis, Der Technischen Fakultät, Universität Erlangen-Nürnberg, Erlangen-Nürnberg, Germany, 2004

[27] Suzuki K., Iwai H., Nishino T., Electrochemical and Thermo-Fluid Modeling of a Tubular Solid Oxide Fuel Cell with Accompanying Indirect Internal Fuel Reforming, Chapter 3 in Sundén B., Faghri M. (eds.), Transport Phenomena in Fuel Cells, WIT Press, UK, 2005

[28] COMSOL Multiphysics 3.5 user guide, Stockholm, Sweden, 2008

[29] Li. P. W., Schaefer L., Chyu M. K., Multiple Transport Processes in Solid Oxide Fuel Cells, Chapter 1 in Sundén B., Faghri M. (eds.), Transport Phenomena in Fuel Cells , WIT Press, UK, 2005